2-21-2002

Keck Spectroscopy and Imaging of Faint Galaxies Identified as Microjansky Radio Sources

Nathan D. Roche
University of Edinburgh, Institute for Astronomy

James D. Lowenthal
University of Massachusetts Amherst, jlowenth@smith.edu

David C. Koo
University of California, Santa Cruz

Follow this and additional works at: https://scholarworks.smith.edu/ast_facpubs

Part of the Astrophysics and Astronomy Commons

Recommended Citation

Keck Spectroscopy and Imaging of Faint Galaxies Identified as MicroJansky Radio Sources

Nathan D. Roche[1,4], James D. Lowenthal[2,5] and David C. Koo[3,6]

[1] *Institute for Astronomy, University of Edinburgh, Royal Observatory, Blackford Hill, Edinburgh, EH9 3HJ, Scotland.*

[2] *Department of Physics and Astronomy, University of Massachusetts, Amherst, MA 01003-4525, USA.*

[3] *UCO/Lick Observatory, Department of Astronomy and Astrophysics, University of California, Santa Cruz, CA 95064, USA.*

[4] `ndr@roe.ac.uk`   [5] `james@velo.astro.umass.edu`   [6] `koo@ucolick.org`

1 February 2008

arXiv:astro-ph/0111371v1 19 Nov 2001

ABSTRACT

We investigate the nature of the faintest radio sources detected in 3 VLA surveys, to F(8.5 GHz) $\sim 8\mu$Jy. Using the Keck Low Resolution Imaging Spectrograph in BRI and the Near Infra Red Camera in K' (2.1μm), we image 51 radio sources, and identify probable optical counterparts for 50. With LRIS spectroscopy, we successfully acquire new redshifts for 17 sources. Combining these with 9 prior redshifts, we can then analyse a sample of 26 μJy sources with spectroscopic redshifts.

Based on this sample of 26, we find the largest contribution, about 60 per cent (15), to be from disk galaxies with high radio to optical ratios, indicating ongoing or very recent starbursts, at redshifts $z = 0$–1. Most of these have large optical luminosites ($M_B \simeq -22 \pm 1$), although two are sub-L^* ($M_B > -20$). About 20 per cent (5) of the sample have relatively low ratios of radio to optical flux, consistent with normal, non-interacting galaxies, all at $z < 0.4$. Four are QSOs, of which one appears to be interacting and shows strong MgII absorption. Two others are very radioluminous giant ellipticals and presumably contain AGN.

All of the 14 non-QSO galaxies with spectra show $H\beta$ and [OII]3727Å emission lines, with luminosities corresponding to star-formation rates (SFRs) of order $\sim 10M_\odot$ yr^{-1}. These SFRs are about an order of magnitude lower than estimated from the radio luminosities. This result may be explained if the galaxies are observed $\sim 10^7$–10^8 yr after a starburst and/or their regions of current star-formation are heavily obscured by dust. Three of the galaxies show strong enough Hδ absorption to be classed as post-starburst or 'e(a)' galaxies.

The Keck spectra are of high enough resolution to provide approximate emission line widths and rotation curves, as well as [OIII]/Hβ ratios ('excitation'). Most of the galaxies (12/14) have high amplitude kinematics (100–400 kms^{-1}), implying large dynamical masses, and moderate excitation ($\sim 0.51 \pm 0.12$), consistent with their morphological appearence as non-AGN, $L \geq L^*$ spirals, of probable near-solar metallicity. The two with low optical luminosities appear to be low-mass galaxies with much higher excitations (~ 2.8), and may be more similar to local HII galaxies than normal spirals.

Key words: galaxies: distances and redshifts – galaxies: evolution – radio: galaxies

1 INTRODUCTION

The radio luminosity of star-forming galaxies is a combination of thermal emission from star-forming regions, discrete synchrotron emission from young supernova remnants, and diffuse synchrotron emission from cosmic rays, which also originate in supernovae. The progenitors of supernovae are short-lived $M \geq 8M_\odot$ stars. The thermal component of radio luminosity will approximately trace the instantaneous star-formation rate (SFR), and the synchrotron component

the very recent SFR, within the previous $\sim 10^8$ yr (Condon 1992; Lisenfeld et al. 1996). In contrast, the optical and near ultraviolet fluxes trace the star-formation integrated over longer periods and are very sensitive to dust extinction, which has no effect at radio wavelengths.

Deep radio surveys are therefore useful in studying galaxy evolution, and especially the importance of short-term, intense bursts of star formation. Benn et al. (1993) found the majority of faint, sub-mJy sources to be star-forming galaxies, rather than AGN. Hammer et al. (1995)

investigated the sources detected in a deep Very Large Array (VLA) radio survey covering one field of the Canada-France Redshift Survey to a limit $F(5.0 \text{ GHz}) \simeq 16\mu\text{Jy}$. Of 36 sources, 34 had probable optical identifications and the CFRS provided redshifts and spectra for 23. The sources were found to be a mixture of (i) ellipticals, presumably with AGN, (ii) disk galaxies with apparently post-starburst spectra, at redshifts out to $z = 1.16$, and (iii) lower redshift, high-excitation emission-line galaxies.

The VLA survey of Windhorst et al. (1995) detected sources to $F(8.5 \text{ GHz}) \simeq 8.8\mu\text{Jy}$ on a field with HST WFPC imaging, and optical counterparts could be identified for 21/22. This sample was found to consist primarily of disk galaxies. Of these, ~ 60 per cent were in close and probably interacting pairs, implying that interaction-triggered starbursts are the dominant mechanism in producing the high radio luminosities. Locally, most radio-selected starburst galaxies are interacting or merging (Smith, Herter and Haynes 1998; Serjeant et al. 2000), as are almost all ultraluminous infra-red galaxies (ULIRGs) (Clements et al. 1996).

Richards et al. (1998) detected $F(8.5 \text{ GHz}) \leq 6.3\mu\text{Jy}$ sources on a VLA image centered on the Hubble Deep Field (HDF), on which redshifts have been measured for most of the brighter ($I < 24$) galaxies. Again, most (70–90%) were star-forming spirals, irregulars and merging galaxies, over a wide $0 < z < 3$ redshift range. The steep number counts and extended $N(z)$ of galaxies in deep radio surveys indicate a strong evolution with redshift in the total SFR (e.g. Haarsma et al. 2000).

In this paper, we investigate a sample of μJy radio-detected galaxies, by performing a multi-passband imaging and spectroscopic survey of three deep VLA fields (including that of Windhorst et al. 1995). We observe in the B, R and (for some galaxies) I bands, and in the near infra-red K' band. The high-quality spectroscopy possible with LRIS yields further information on the nature of these galaxies. First, Lisenfeld et al. (1996) predict, at the end of a starburst, the thermal component of radio emission will decline within ~ 20 Myr but the enhanced synchrotron emission will maintain a high radio luminosity for at least ~ 70 Myr. This means that if starbursts are relatively brief (< 100 Myr), a radio-selected sample would contain a significant fraction of recent post-starburst galaxies – which could be identified from their strong Hδ absorption (e.g. Delgado, Leitherer and Heckman 1999; Poggianti and Wu 2000).

Second, the luminosities of some emission lines (e.g. Hβ) trace the immediate SFR, and hence the ratio of line to radio luminositity would be sensitive to dust extinction and/or starburst age. Third, the ratio of the [OIII]5007Å and Hβ fluxes ('excitation') is sensitive to the Hubble type and metallicity of a galaxy and may reveal an AGN contribution (Tresse et al. 1996; Sodre and Stasinska 1999). Fourth, the high spectral resolution will enable us to derive kinematic information from the 2D (spatial/spectral) emission-line profiles.

Section 2 gives details of our data, and Section 3 their reduction. Section 4 describes the identification of the optical counterparts of the radio sources, lists positions and magnitudes and shows optical images. Section 5 presents our source spectra, and Section 6 discusses optical and radio luminosities and colours. In Section 7 we identify the galaxies in close or interacting pairs, in Section 8 interpret the spec-

tral line equivalent widths, and in Section 9 use line profiles to investigate galaxy kinematics. Section 10 is an overview and discussion of all our results on $\sim 10\mu$Jy sources.

Throughout, magnitudes are given in the AB system, defined such that $m_{AB} = 48.60 - 2.5 \log_{10} f_\nu$ where f_ν is in erg s^{-1}Hz^{-1}, or, equivalently, $f_\nu = 3631 \times 10^{-0.4 m_{AB}}$ Jy. For the passbands of observation, $B_{AB} = B_{Vega} - 0.048$, $R_{AB} = R_{Vega} + 0.175$, $I_{AB} = I_{Vega} + 0.483$, $K'_{AB} = K'_{Vega} + 1.791$. Quantities dependent on Hubble's Constant are given in terms of $h_{50} = H_0/50$ km s^{-1}.

2   OBSERVATIONAL DATA

2.1   Radio Surveys

This study is based on the published source catalogs from three deep radio surveys, of fields originally studied in the Leiden Berkeley Deep Survey (Windhorst, van Heerde and Katgert 1984). The radio observations were carried out using the National Radio Astronomy Observatory Very large Array (VLA) in San Augustin, New Mexico. The first survey is of the 'Lynx2' field, centered at R.A. $08^h 45^m 04^s$ Dec 44:34:05 (equinox 2000.0 is used throughout). VLA observations of 63 hours in December 1989 and January 1990, at 8.44 GHz, gave a noise level of $\sigma = 3.21\mu$Jy and an estimated 14.5μJy completeness limit. Windhorst et al. (1993) cataloged 46 sources detected at $\geq 4\sigma$, and we adopt their source numbers (prefixed '16V'). Of these, only 14 belong to a 'complete sample' which have a peak flux density $\geq 14.5\mu$Jy and are within 4.59 arcmin of the field centre. The names of sources not in the complete sample are suffixed with '*'. The source '16V29A*' was considered to be part of the same extended object as 16V29, and here the fluxes are combined into a single 16V29 source.

The second, and deepest, VLA survey is centered on the 'Lilly field' of the HST Medium Deep Survey, R.A. $31^h 12^m 17^s$ Dec $+42$:38:06. VLA observations, again at 8.44 GHz, totalled 159 hours between October 1993 and January 1995, giving a noise level $\sigma = 1.5\mu$Jy and an estimated completeness limit 8.8μJy. Windhorst et el. (1995) list 24 sources and identify their optical counterparts on WFPC images; we adopt their source numbers, adding a prefix 'L'. However, two of these (L14 and L22) are actually non-detections and not considered here. We retain L20 and L21, which are detections but have fluxes 7–8.8μJy, just below the completeness limit.

Thirdly, we include some sources from the larger area but less deep survey of Weistrop et al. (1987), in which a field known as SA68 (R.A. $23^h 59^m 15^s$ Dec 14:55:00) was observed at 5.0 GHz for 40 hours, detecting 9 sources to a completeness limit 60μJy (~ 40–45μJy at 8.44 GHz). We adopt their nomenclature, abbreviating the 'SA68' prefix to 'S'.

The VLA surveys of Lynx2 and SA68 have only FWHM ~ 10 arcsec resolution – hence, although Windhorst et al. (1993) considered most Lynx2 source positions accurate within < 2 arcsec, we might expect a few to have offsets of up to ~ 7 arcsec. On the Lilly field the use of VLA C-configuration improved the FWHM to ~ 3 arcsec.

2.2 Optical Imaging

Our optical imaging observations were performed using the Low Resolution Imaging Spectrometer (LRIS), on the Keck telescope in Hawaii (Oke et al. 1995). This camera, is fitted with a 2048×2048 pixel CCD, giving a $\sim 7 \times 7$ arcmin field-of-view with a pixelsize 0.215 arcsec. LRIS observations were taken on the 3rd and 4th of January 1995, and made use of B ($\lambda_{eff} = 4377$Å, FWHM 919Å), R ($\lambda_{eff} = 6417$Å, FWHM 1185Å) and I ($\lambda_{eff} = 8331$Å, FWHM 3131Å) filters.

Pointing at R.A. $08^h 45^m 00^s$ Dec 44:34:59, we imaged the central part of the Lynx2 field, for 8×300 sec exposures in B, 11×300 sec in R and 6×300 sec in I. The Lilly field, where the LRIS CCD covers the whole area of the Windhorst et al. (1995) survey, was observed for 2×300 sec in each of B and R. The SA68 radio sources are more widely spread and it was necessary to observe them individually. A field centered on SA68:10 was imaged for 2×300 sec in B, 4×300 sec in R and 3×300 sec in I, and three other fields in I only, for a single 300sec exposure – the first containing SA68:02 and SA68:04, the second SA68:09 and the third SA68:12.

2.3 Near Infra-Red Imaging

Using the Keck telescope Near Infra-Red Camera (NIRC) (Matthews and Soifer 1994), we observed the sources in the K' passband ($\lambda_{eff} = 2.124\mu$m FWHM 0.337μm), on the 8th of January 1996. NIRC is fitted with a 256×256 pixel indium-antimonide (InSb) detector, providing a 37.5 arcsec field of view with pixelsize 0.15 arcsec. Most sources were observed for 5 consecutive spatially-dithered exposures of 60 sec (each exposure was in turn made up of 6 co-added 10 sec integrations); a few received 10 exposures.

2.4 Optical Spectroscopy

Spectroscopic observations were performed using LRIS, on the same nights as the direct imaging, and made use of multi-slit masks or, for a few galaxies, single long slits. The spectrograph is sensitive at 4000–10000Å, but only a ~ 2600Å range is observed for each source, the starting wavelength depending on the slit position. With the 600 lines mm^{-1} grating, the wavelength dispersion is 1.27Å pixel^{-1} with resolution 3.1Å FWHM.

The Lynx 2 field multi-slit mask had 22 slits, of which 12 were positioned on likely optical counterparts for the radio sources and the remainder on other galaxies for a separate redshift survey, and received 11×1000 sec exposures. Four Lynx2 sources were observed with a single long slit and either one or two 1800 sec exposures. The Lilly field multi-slit mask had 11 slits, all positioned on radio sources, and received 3×1800 sec exposures. The long slit was again used for five of the SA68 sources, with 1000 or 1800 sec exposures.

3 DATA REDUCTION AND ANALYSIS

3.1 Optical Data

The LRIS images were debiased, and flat-fielded using 'pyraf' routines developed by Dan Kelson. Multiple exposures were averaged, with rejection of cosmic rays using the 'nukecr' routine of Luc Simard. The stacked B, R and I

frames of the Lynx2 field, and the B and R frames of the Lilly field, were then positionally registered.

Sources were detected and catalogued using SExtractor (Bertin and Arnauts 1996) in 'double-image mode', meaning that one frame is used for source detection but the fluxes are measured from the same positions on a second. For each of the fields we coadded the exposures in different passbands (weighting each by the inverse of its rms) to give combined 'BRI' and 'BR' images, which were used for source detection. SExtractor measured 'Kron-type' total magnitudes from the single-passband images within elliptical apertures, which are fitted to each source on the detection frame. The aim of this was (i) to optimize the detection of faint sources by combining all the data, and (ii) to obtain more reliable colours, by positionally matching the photometric apertures used in different passbands.

For the Lynx2 field, the usable area covered in all 3 passbands was 5.03×6.93 arcmin. The resolution was estimated, from the SExtractor FWHM of objects classed as stars, as 1.34 ± 0.05 (B), 1.45 ± 0.03 (R) and 1.23 ± 0.03 (I) arcsec, and the sky noise σ_{sky} as $26.97(B)$, $27.23(R)$, $26.63(I)$ mag arcsec^{-2}. Our Lilly field image covered 5.63×7.21 arcmin, with somewhat poorer resolution, estimated as 3.03 ± 0.11 (B) and 2.07 ± 0.11 (R) arcsec, and is a little less deep, with σ_{sky} of $26.39(B)$ and $26.47(R)$ mag arcsec^{-2}.

Sources were detected as areas of 14 or more contiguous pixels above a threshold of $1.0\sigma_{sky}$ (Lynx2 field) or $1.1\sigma_{sky}$ (Lilly field) above the sky background on the detection frame. Detections were deblended with a minimum contrast threshold of 0.02. This gave a total of 2462 detections on the Lynx2 field, with source counts turning over at $B > 26.5$, $R > 26$ and $I > 26$, and 1506 on the Lilly field, with counts turning over at $B > 25.5$ and $R > 25.5$. For the SA68:10 field, the B R and I frames were coadded and sources detected above a $1.25\sigma_{sky}$ threshold. The I-band exposures of the other three SA68 sources were analysed as single images, again with $1.25\sigma_{sky}$ thresholds.

Star-galaxy classification was performed using plots of FWHM against magnitude, on which the stellar locus was separable from the larger galaxies to $I = 20.4$ on Lynx2 and $B = 21.2$ on the Lilly field. Fainter detections were classed as galaxies.

3.2 Near Infra-Red Data

The NIRC K' images were reduced using IRAF 'dimsum' (created by P. Eisenhardt, M. Dickinson et al.), which positionally registered and stacked the dithered exposures, rebinning to 0.0375 arcsec pixels, while subtracting the sky background and removing cosmic rays. The resolution of the stacked frames was estimated from stellar images as 0.74 arcsec FWHM, significantly better than the BRI data. Objects were detected and catalogued using SExtractor with a minimum area 16 pixels and a threshold $2.25\sigma_{sky}$ ($\sigma_{sky} = 21.7$–22.4 mag arcsec^{-2}), which typically gave 5–10 detections per NIRC frame.

3.3 Photometric Calibration

Photometric zero points were calculated for the Lynx2 B, R and I images using ~ 50 previously photometrically catalogued stars on the observed field. These zeropoints were

then applied to the Lilly and SA68 data with corrections for the differences in observation airmass (assuming $\Delta B = 0.233X$, $\Delta R = 0.067X$, $\Delta I = 0.014X$ from a tabulated extinction curve). Magnitudes were also corrected for Galactic extinction, as given by the NASA/IPAC Extragalactic Database (in the B-band, 0.112 mag for Lynx2, 0.058 for the Lilly field and 0.226 for SA68). The K' zeropoint was determined from two standard stars, FS 5 ($K' = 13.342$) and FS 21 ($K' = 13.115$), observed on the same nights as the galaxies.

Photometric errors in R, I and K' magnitudes are generally ≤ 0.1 mag for the brighter, $R < 23.5$, galaxies. In the B-band the errors are ≤ 0.1 mag to $B \sim 22.8$ but for fainter B magnitudes may exceed ~ 0.2 mag.

3.4   Spectroscopic Data

Reduction of the LRIS multi-slit and single-slit spectroscopic data began with debiasing and cleaning of bad pixels, using the 'pyraf' routines of Dan Kelson. Multiple exposures were positionally registered to the nearest integral pixel, and cosmic-rays removed using 'nukecr'. The 'rmydist' routine of Dan Kelson was used to fit and remove (by rebinning) the slight y (spatial) direction distortion of LRIS spectra.

The first exposure of the Lynx2 mask was divided into 22 strips, each containing the light from one of the spectrograph slits. Each of the strips was analysed separately, following essentially the methods of Mallen-Ornelás (2000). A wavelength calibration was fitted to the sky emission lines on each strip, with rms residuals of 0.5–0.7Å. LRIS spectra also suffer a y-dependent distortion in the x-direction, resulting in the sky lines being slanted from the vertical. To correct for this, the wavelength calibration was refitted to the sky lines at several y positions on each strip, a two-dimensional function was then refitted with IRAF 'fitcoords', and (IRAF 'transform') was used to rebin each line of the spectra to a common and linear λ scale.

This transform was then applied to the subsequent exposures of the same spectrum. There were sometimes small (~ 1Å) offsets in λ between the transformed exposures. These were measured using IRAF 'xregister', and the pre-transform strips were then re-transformed, with the offsets subtracted from the x_1 and x_2 parameters. This reduced offsets between exposures to < 0.2Å. The same procedure was then applied to the 11 strips of the multi-slit Lilly field mask and to the much broader strips of the long-slit images. The multiple exposures of each spectrum were combined by simple averaging, and then sky-subtracted using IRAF 'background' – at each position on the wavelength (x) axis, 4th-order functions were fitted to the variation of the sky in the spatial (y) direction (excluding the region where the galaxy spectrum is visible), and then subtracted, to give a sky-subtracted 2D spectrum. One-dimensional spectra were then extracted by using IRAF 'apall' to perform (variance-weighted) extractions in apertures of width 12–20 pixels (2.6–4.3 arcsec), centered on each galaxy spectrum and covering its full width in the spatial direction. The extracted spectra are shown in Section 5 below.

4   OPTICAL COUNTERPARTS OF THE RADIO SOURCES

4.1   Identification

The areas covered by our LRIS and/or NIRC images contain a total of 51 catalogued VLA sources, of which 40 are in a 'complete sample' (the 16V sources listed as being in the complete sample, plus all the others except L20 and L21). Many of these coincide obviously with a bright galaxy, but in other cases there may be several fainter galaxies within the 'error box'. We determine which galaxies are the most probable identifications as described below.

(i) For both Lynx2 and Lilly fields, we used the positions of faint stars from the USNO catalog – of which ~ 20 were detected on each frame area - with the IRAF 'pltsol' routine to derive accurate astrometric transforms, with RMS residuals ~ 0.6 arcsec.

(ii) These astrometric transforms were used to convert the centroid positions of the radio sources (Windhorst et al 1993, 1995) to pixel co-ordinates on the optical CCDs.

(iii) Using SExtractor, an integral number count $n(m)$ of objects classed as galaxies is determined for each LRIS field, as a function of optical magnitude (for all passbands used).

(iv) For each galaxy detected within 7 arcsec of one of the radio sources, a probability,

$$P = 1.0 - \exp(-\pi r^2 n(m))$$

is estimated, where r is the distance from the radio source centroid to the galaxy position, and $n(m)$ the integral number count (surface density) of galaxies brighter than the galaxy under consideration (magnitude m). P is then the probability that a galaxy of similar or greater brightness would, entirely by chance, lie at a similar or closer distance from the radio source. The 'best' optical counterpart is then the galaxy with the lowest P.

The analysis was repeated with $n(m)$ from different optical passbands. Galaxies with $P < 0.05$ in one or more passbands are then considered to be very probable optical IDs. For each source the reliability of the identification is represented as ID class I ($P < 0.05$), II ($0.05 < P < 0.1$) or III ($P > 0.1$), where P is the lowest value of the 2 or 3 passbands.

In total we find 39 IDs of class I (with $\langle r \rangle = 1.4$ arcsec), 7 of class II ($\langle r \rangle = 3.9$ arcsec) and 4 of class III ($\langle r \rangle = 4.7$ arcsec). Using our astrometric transforms, the optical ID positions are converted to RA/Dec co-ordinates, listed in Table 1 together with the radio centroid co-ordinates from the VLA data. Only one of the 51 sources, L12, had no detectable counterpart within 7 arcsec of the radio position on either the LRIS or NIRC images. Windhorst et al. (1995) thought L12 might be part of the large L13 galaxy, and we do not consider this 'source' any further.

To investigate the reliabilty of our ID technique, we performed simulations in which radio sources were assigned random positions against a background consisting of the Lynx2 galaxies. Simulated optical counterparts were then added with optical magnitudes and separations from the radio sources randomly drawn from the magnitudes and separations of the 'class I' IDs. The simulated radio sources were then 'P-tested' against catalogs consisting of the background galaxies plus the simulated counterparts.

Table 1. Co-ordinates (equinox 2000.0) of the VLA radio sources and of the galaxies identified as most probable optical counterparts, separation r of the radio and optical positions, classes (I–III) for the reliability of the ID, 8.44 GHz fluxes, magnitudes (AB system) and approximate morphological types of the galaxies (d=disk, b=bulge, i=irregular, Q=QSO, p=pair d=disturbed).

Radio Source	Radio position R.A.	Dec.	Optical position R.A.	Dec.	r arcsec	ID class	8.44 GHz flux μJy	B mag	R mag	I mag	K' mag	Mo. type
16V08	8:44:43.90	44:34:01.22	8:44:43.75	44:33:59.74	2.2	II	58.0 ± 14.3	24.45	24.53	24.57	-	d
16V10*	8:44:45.90	44:33:03.21	8:44:45.56	44:32:59.82	5.0	III	76.1 ± 23.1	25.28	24.27	23.18	20.48	d
16V13	8:44:50.39	44:35:55.37	8:44:50.62	44:35:54.36	2.6	I	62.1 ± 15.8	22.54	22.16	21.66	20.51	Qp
16V15*	8:44:53.30	44:32:37.90	8:44:53.24	44:32:39.11	1.4	I	21.4 ± 5.6	23.01	21.90	21.56	19.62	dp
16V16*	8:44:56.68	44:33:17.01	8:44:56.61	44:33:15.68	1.6	I	14.5 ± 3.9	25.27	23.86	22.88	20.25	d
16V17	8:44:56.82	44:34:51.11	8:44:56.82	44:34:51.26	0.2	I	20.2 ± 4.3	18.42	18.58	19.21	18.52	Q
16V18*	8:44:56.91	44:37:44.70	8:44:56.73	44:37:43.76	2.3	I	75.3 ± 23.8	22.94	23.69	23.80	-	dp
16V19*	8:44:56.80	44:31:35.11	8:44:56.98	44:31:32.44	3.3	I	24.8 ± 6.8	22.10	22.35	22.02	-	d
16V20*	8:44:57.19	44:34:31.69	8:44:57.32	44:34:31.62	1.3	I	14.2 ± 3.8	24.70	22.30	21.20	19.25	d
16V21	8:44:57.82	44:33:15.75	8:44:58.22	44:33:13.46	4.9	I	50.4 ± 5.5	22.59	22.98	23.09	23.07	dp
16V22	8:44:59.03	44:33:49.28	8:44:59.00	44:33:44.00	5.3	II	20.6 ± 3.6	23.18	22.65	22.59	22.53	d
16V23*	8:44:59.30	44:35:29.66	8:44:59.36	44:35:30.15	0.8	I	19.2 ± 4.6	23.51	22.67	21.64	-	d
16V24	8:44:59.93	44:33:49.83	8:45:00.28	44:33:49.20	3.7	II	32.2 ± 3.7	23.72	24.15	23.85	23.91	d
16V25	8:45:05.48	44:34:15.62	8:45:05.48	44:34:15.14	0.5	I	31.5 ± 3.6	24.91	22.92	21.89	19.46	d
16V26	8:45:05.57	44:33:58.62	8:45:05.61	44:33:56.56	2.1	II	35.3 ± 3.6	24.91	25.39	24.75	21.54	d
16V28	8:45:06.17	44:35:19.68	8:45:06.13	44:35:19.38	0.6	I	110.0 ± 10.0	15.94	15.36	15.68	-	dp[1]
16V29	8:45:06.32	44:36:24.68	8:45:06.04	44:36:23.93	3.1	I	155.6 ± 24.3	16.43	15.75	15.85	-	dp
16V30*	8:45:07.77	44:33:49.69	8:45:07.91	44:33:51.60	2.4	I	13.8 ± 3.4	22.29	20.94	20.33	18.37	dp
16V31	8:45:08.30	44:34:40.37	8:45:08.35	44:34:38.58	1.9	I	62.4 ± 5.1	22.86	21.44	20.90	18.73	d
16V34	8:45:14.46	44:34:51.53	8:45:14.33	44:34:50.97	1.6	I	31.0 ± 5.9	21.28	20.29	19.90	18.10	dd
16V35*	8:45:17.07	44:35:18.58	8:45:16.92	44:35:24.52	6.2	II	25.4 ± 7.5	22.84	23.07	22.86	22.49	d
16V36	8:45:19.28	44:46:46.26	8:45:19.49	44:35:42.87	4.1	I	78.10 ± 14.90	20.71	19.39	19.00	17.40	dp
L1	13:12:14.45	42:38:21.6	13:12:14.55	42:38:21.52	1.1	I	9.8 ± 2.0	23.08	23.31	$22.23^{[2]}$	20.59	d
L2	13:12:14.51	42:37:31.1	13:12:14.63	42:37:31.47	1.4	I	8.8 ± 2.0	25.27	25.15	$25.62^{[2]}$	-	d
L3	13:12:15.08	42:37:02.6	13:12:15.15	42:37:01.84	1.1	I	12.1 ± 2.0	20.71	20.19	$21.13^{[2]}$	19.39	dp
L4	13:12:15.29	42:39:00.9	13:12:15.23	42:39:00.56	0.7	I	27.3 ± 2.0	17.87	18.45	$18.21^{[2]}$	-	Q
L5	13:12:16.07	42:39:21.3	13:12:16.49	42:39:19.9	4.9	III	31.8 ± 2.0	25.09	24.18	$24.82^{[2]}$	-	d
L6	13:12:17.17	42:39:12.5	13:12:17.19	42:39:11.72	0.8	I	23.2 ± 2.0	21.94	20.85	$20.47^{[2]}$	18.78	dp
L7	13:12:17.59	42:39:30.6	13:12:17.36	42:39:26.99	4.5	III	15.2 ± 2.0	25.58	25.57	$25.22^{[2]}$	21.09	d
L8	13:12:18.30	42:39:08.1	13:12:18.28	42:39:08.82	0.8	I	15.3 ± 2.0	25.88	25.24	$25.62^{[2]}$	23.13	dp
L9	13:12:18.46	42:38:43.9	13:12:18.44	42:38:43.50	0.5	I	21.8 ± 2.0	23.20	21.86	$20.70^{[2]}$	18.68	dp
L10	13:12:19.57	42:38:33.0	13:12:19.58	42:38:32.80	0.3	I	17.8 ± 2.0	22.27	21.42	$20.87^{[2]}$	19.60	d
L11	13:12:20.16	42:37:03.4	13:12:20.23	42:37:04.33	1.2	I	9.6 ± 2.0	$28.81^{[3]}$	$25.03^{[3]}$	$> 25.72^{[2]}$	22.37	d
L12	13:12:20.02	42:39:23.4	[4]		-	-	11.8 ± 2.0	[4]	[4]	[4]	[4]	-
L13	13:12:21.04	42:39:23.3	13:12:21.02	42:39:22.26	0.3	I	10.1 ± 2.0	19.69	18.80	$18.40^{[2]}$	17.19	d
L15	13:12:21.33	42:37:22.9	13:12:21.31	42:37:22.69	0.3	I	10.1 ± 2.0	19.34	18.68	$18.22^{[2]}$	17.54	d
L16	13:12:21.83	42:38:27.3	13:12:21.82	42:38:26.68	0.6	I	16.6 ± 2.0	21.80	21.88	$23.14^{[2]}$	21.52	dp
L17	13:12:22.49	42:38:14.1	13:12:22.39	42:38:13.62	1.3	I	11.5 ± 2.0	20.65	20.44	$19.99^{[2]}$	19.56	Q
L18	13:12:23.24	42:39:08.6	13:12:23.22	42:39:07.42	1.2	I	22.6 ± 2.0	21.82	20.87	$19.71^{[2]}$	18.04	dp
L19	13:12:23.67	42:37:11.9	13:12:23.70	42:37:11.60	0.4	I	24.4 ± 2.0	20.94	19.70	$19.18^{[2]}$	17.68	dp
L20	13:12:24.11	42:38:05.2	13:12:23.74	42:38:06.69	4.5	III	8.3 ± 2.0	24.50	24.53	$24.82^{[2]}$	21.10	dp
L21	13:12:24.42	42:37:05.2	13:12:24.41	42:37:11.07	5.9	I	7.0 ± 2.0	23.30	21.36	$21.02^{[2]}$	19.20	dp
L23	13:12:25.74	42:39:41.5	13:12:25.65	42:39:38.47	3.2	II	380.0 ± 2.0	23.83	23.79	$> 21.72^{[2]}$	21.16	dd
L24	13:12:27.50	42:38:00.3	13:12:27.49	42:38:00.42	0.2	I	22.4 ± 2.0	21.43	20.27	$20.27^{[2]}$	18.13	dd
S2	00:17:40.96	15:51:09.3	00:17:40.89	15:51:11.6	2.5	II	378.8 ± 29.1	-	-	25.18	22.49	d
S4	00:17:41.81	15:50:03.4	00:17:41.75	15:50:03.2	1.0	I	270.2 ± 20.3	$23.42^{[5]}$	$21.84^{[5]}$	20.96	18.98	b
S5	00:17:43.85	15:54:05.0	00:17:43.78	15:54:04.2	1.3	I	843.9 ± 51.8	$21.68^{[5]}$	$19.27^{[5]}$	-	17.24	bp
S9	00:17:59.66	15:41:59.2	00:17:59.59	15:41:57.5	2.0	I	$5725. \pm 175.$	-	-	22.15	19.19	bp
S10	00:18:03.75	15:49:04.0	00:18:03.66	15:49:04.6	1.4	I	53.0 ± 12.1	23.08	22.90	22.23	20.87	dd
S11	00:18:07.61	15:48:27.8	00:18:07.63	15:48:27.2	0.7	I	51.4 ± 11.0	$19.26^{[5]}$	$17.72^{[5]}$	-	16.36	b
S12	00:18:18.83	15:54:35.4	00:18:18.78	15:54:35.6	0.7	I	568.2 ± 51.0	-	-	21.53	19.36	dp

Notes: -: Not observed in this passband. [1]: Pair with 16V29. [2]: I_{HST} magnitude from Windhorst et al. (1995). [3]: A significant detection on the NIRC but not on the LRIS image – listed B and R magnitudes are estimated from aperture photometry at the position of the K' detection. [4]: No counterpart visible within 7 arcsec in either LRIS or NIRC image. [5] Estimated from the B_J and F photometry of Munn et al. (1997) *: Suffix to name of Lynx2 sources not in the 'complete' sample of Windhorst et al. (1993).

The test selected the simulated counterpart, rather than one of the uncorrelated background galaxies, as the best ID for 91 per cent of the sources.

4.2   Magnitudes and Morphologies

We examine the NIRC K'-band frames and identify the galaxies considered the most likely optical counterparts of the radio sources. Table 1 gives the apparent magnitudes as measured using SExtractor, together with RA/Dec coordinates of the optical IDs (from our astrometric transforms) and the radio centroids. Two galaxies, 16V36 and L21, were detected as single sources in our analysis of the LRIS frame, but appear double-peaked, and are split into two detections on the NIRC data. For these we give in Table 1 the K' mag of the two components combined, and consider the two nuclei separately in Section 7. For S4, S5 and S11, we estimate B and R magnitudes from the B_J and R_F photometry of Munn et al. (1996), using magnitude transforms (Fukugita, Shimasaku and Ichikawa 1995) appropriate for ellipticals (on the basis of the red colours and bulge profiles of these galaxies).

Table 1 gives the observed 8.44 GHz fluxes from Windhorst et al. (1993, 1995), for Lynx2 and Lilly field sources. For the SA68 sources, 8.44 GHz fluxes are estimated from the 5.0 GHz fluxes of Weistrop et al. (1987), assuming the Condon (1992) SED, for which $F(8.44)/F(5.0) = 0.73(0.76)$ at $z = 0(1)$.

Greyscale plots of the identified galaxies will be included in the published version (MNRAS). For each of the optical IDs, we examine the LRIS and/or NIRC images by eye, and fit isophotes and radial profiles to the K'-band images using IRAF 'isophote.ellipse'. On this basis we assign approximate morphological classifications (Table 1).

Most of the galaxies have approximately exponential (disk) profiles and are classed here as (i) apparently 'normal' disks ('d') - isolated, symmetric, with single nuclei, (ii) disturbed disks ('dd'') with visible asymmetry or isophotal twist, or (iii) disk galaxies in close pairs or groups or with double nuclei ('dp'), which may be interacting or merging. Of course, some galaxies in class 'd' may have interaction features not visible in these ground-based images. In addition, there are QSOs seen as high surface brightness point sources ('Q'), one QSO within an apparently merging system ('Qp'), bulge galaxies ('b'), i.e. with profiles closer to the form exp $[-r^{0.25}]$ than exp $[-r]$, and bulge galaxies in close pairs ('bp'). Our classifications of the Lilly field sources are in general agreement with Windhorst et al. (1995).

5   SPECTROSCOPY: RESULTS

On the Lynx2 multi-slit mask, 12 slits were dedicated to 16V radio sources. Spectra were successfully extracted for 16V10*, 13, 15*, 17, 25, 31, 34 and 36. We failed to obtain spectra for 16V21, 22 and 35 due to inaccurate slit positions – the slits had been positioned on the VLA co-ordinates, which were a few arcsec offset from the faint optical counterparts. In the case of 16V08, the slit position appeared correct but the galaxy was too faint ($R = 24.53$) to see any significant spectrum. The faintest successfully observed galaxy was 16V10*, with $R = 24.27$. The spectroscopic slit

covered only one of the two nuclei of the merging 16V36, while for the paired 16V15* we obtained spectra for both the radio ID and its companion (hereafter 16V15B).

An additional long-slit observation provided a spectrum for the previously missed 16V22, and also 16V24, but the latter proved too faint ($R = 24.15$) to identify any spectral features. The Lilly field multi-slit mask provided good spectra for L4, 6, 9, 18, 21, and 24. Objects L10, 13 and 16 were missed due to inaccurate slit positions (a discrepancy between VLA and optical astrometric solutions), while L5 ($R = 24.18$) and L23 ($R = 23.79$) were too faint. Long-slit spectroscopy of SA68 sources provided spectra for S4 and S10. S2 was also observed but, with $I = 25.18$, was too faint.

We have spectroscopically observed 22 of the 50 radio IDs, and obtained 'good' spectra for 17, the remaining 5 being too faint. All except for 16V10*, 16V15* and L21 belong to 'complete' radio-source lists. The spectra were examined using an enhanced version of IRAF 'splot', to identify significant emission and absorption features, and measure the equivalent widths (hereafter EWs) and FWHM (from a Gaussian fit) of emission lines. Redshifts were determined from the one or two strongest emission lines. Table 2 gives the EWs (errors are typically 0.5–1.0Å; see Section 8).

We measure redshifts from the 17 'good' spectra, and consider these to be reliable, as all are based on multiple spectral features. In addition, Windhorst et al. (1995) give spectroscopic redshifts of $z = 0.322$ for L3, $z = 0.302$ for L13, $z = 0.180$ for L15, $z = 2.561$ for the QSO L17, and $z = 0.401$ for L19, Weistrop et al. (1987) give $z = 0.168$ for S11 and Munn et al. (1997) $z = 0.3493$ for S5, $z = 0.0531$ for 16V28 and $z = 0.0535$ for 16V29. Thus in total we have a subsample of 26 radio sources with known redshifts, hereafter the 'redshift sample'.

The redshift sample cannot be described as purely radio-selected, as there is an additional optical selection bias, approximately in the R-band (about the centre of the spectrometer wavelength range). The magnitudes of the radio IDs extend faintwards of $R \sim 25$, while all the redshift sample galaxies have $R < 24.3$, and all the redshifts from previous data are for $R < 20.5$ galaxies. Figure 2 illustrates the optical bias of the redshift sample by comparing its R magnitude distribution with that of all the radio IDs.

Of the 17 radio IDs with LRIS spectra, 14 are emission-line galaxies and 3 are QSOs. Emission features typically observed are Hβ and [OIII]5007Å, together with [OIII]4959Å, and at the higher redshifts, [OII]3727Å. Some galaxies show Balmer lines Hγ (in either emission or absorption), and Hδ, and the broader absorption features H3969Å and K3934Å. Only 16V10* appears to show Hδ in emission and the reality of the line is is uncertain as it is only 2–3σ and, although its wavelength is consistent with the redshift from the other features, it is also within ~ 3Å of a sky line. The [OII]3727 line of 16V10* appears on the 1D plot to be 'lost' amongst sky lines, but the 2D spectrum reveals it to be very different from the sky features and a real emission line.

The companion galaxy 16V15B shows only absorption lines, including G4304Å and Hγ (EW ~ 1.0Å), the latter giving $z = 0.4855$ with a line-of-sight velocity only 71 ± 33 km s^{-1} greater than 16V15. Another pair, 16V22 and 16V34 are also at closely similar redshifts, with $\Delta(v) = 35 \pm 17$ km

Table 2. Redshifts (errors ±0.0001) and rest-frame EWs (in Å, emission positive, absorption negative) of significantly detected spectral lines, for galaxies (above) and QSOs (below) identified as radio sources.

Galaxies

Source	z	[OII] 3727	Hδ	Hγ	Hβ	[OIII] 5007
16V10*	1.0838	7.37	2.83?	-	-	-
16V15*	0.4854	-	-	1.33	9.59	6.16
16V22	0.4259	-	-	5.19	8.92	30.19
16V25	0.7273	8.78	-1.94	<	<	<
16V31	0.4977	-	-8.14	-2.14	3.09	6.29
16V34	0.4257	-	-	<	4.54	3.37
16V36	0.4073	-	-	<	4.82	2.28
L6	0.4946	-	-	-	7.83	3.81
L9	0.6986	15.45	-4.44	<	8.61	6.74
L18	0.7648	5.68	-5.22	<	<	<
L21	0.2905	-	-	-	12.30	40.19
L24	0.3155	-	-	-	4.05	2.70
S4	0.7125	7.54	-2.51	<	<	<
S10	0.9923	52.50	<	-	-	-

QSOs

Source	z	[NeIV] 2424/6	MgII 2796/2804	OIII 3341
16V13	1.8330	-	-18.68, -16.08	
16V17	1.6550	-	-	0.76
L4	2.5580	0.54, 0.39	-	-

(-: line is outside observed λ range. <: line is not detectable at 2σ level).

s^{-1}, but are separated by 180 arcsec ($\simeq$ 1.39 Mpc) on the sky.

    The QSO spectra may show MgII2796.4, 2803.5Å (as broad emission and/or narrow absorption lines) and/or narrow [NeIV]2424, 2426Å or OIII3341Å emission.

6   COLOURS AND LUMINOSITIES

6.1   Optical Flux

We have identified likely optical counterparts for 51 radio sources, and of these 44 are observed in the R-band. Figure 3 shows their R magnitude against 8.44 GHz flux, with error bars.

    An important question is whether radio-selected galaxies tend to be bluer (e.g. from star-formation) or redder (e.g. from dust) than other galaxies at similar apparent magnitudes. Figure 4a compares the $B - R$ distributions of the 47 radio source IDs with B and R magnitudes, with that of all 519 $R < 24.0$ galaxies (including the radio IDs) on the combined Lynx2 and Lilly fields. The radio-selected sample contains a higher proportion of $B - R \sim 1$ galaxies, but the mean $B - R$ is only slightly redder, 0.71 compared to 0.62; only 3/47 of the radio source IDs are very red ($B - R > 2$), while the proportion (16/44) of very blue ($B - R < 0.2$) galaxies is similar to the $R < 24.0$ sample. Figure 4b compares the $B - I$ distributions of the 24 radio IDs observed in B and I with that of all $R < 24.0$ galaxies on Lynx2 - these are again very similar.

    We conclude from this the radio detections generally have similar colours to optically-selected star-forming galax-
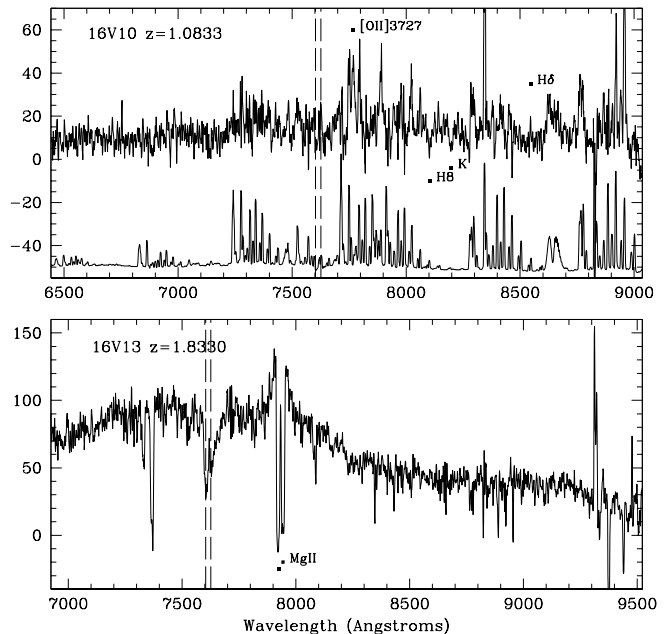
Figure 1. Spectra of the 17 radio sources and the companion galaxy 16V15B. Significantly detected lines are marked, above (emission) and below (absorption) the spectra. The x-axis is observer-frame observer-frame, and the y-axis scale is counts pixel^{-1} (not flux calibrated). The spectrum of the sky background (which can produce spurious features in the galaxy spectra) is shown underneath 16V10*. Vertical dashed lines show the wavelengths of sky absorption features.
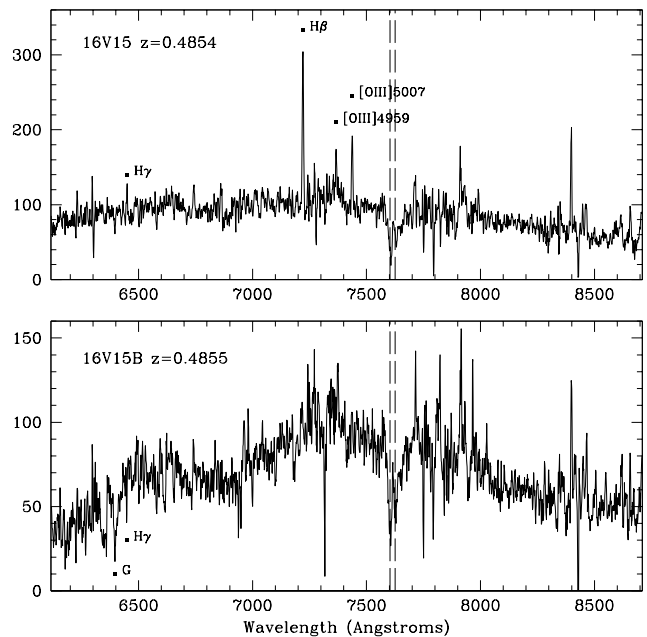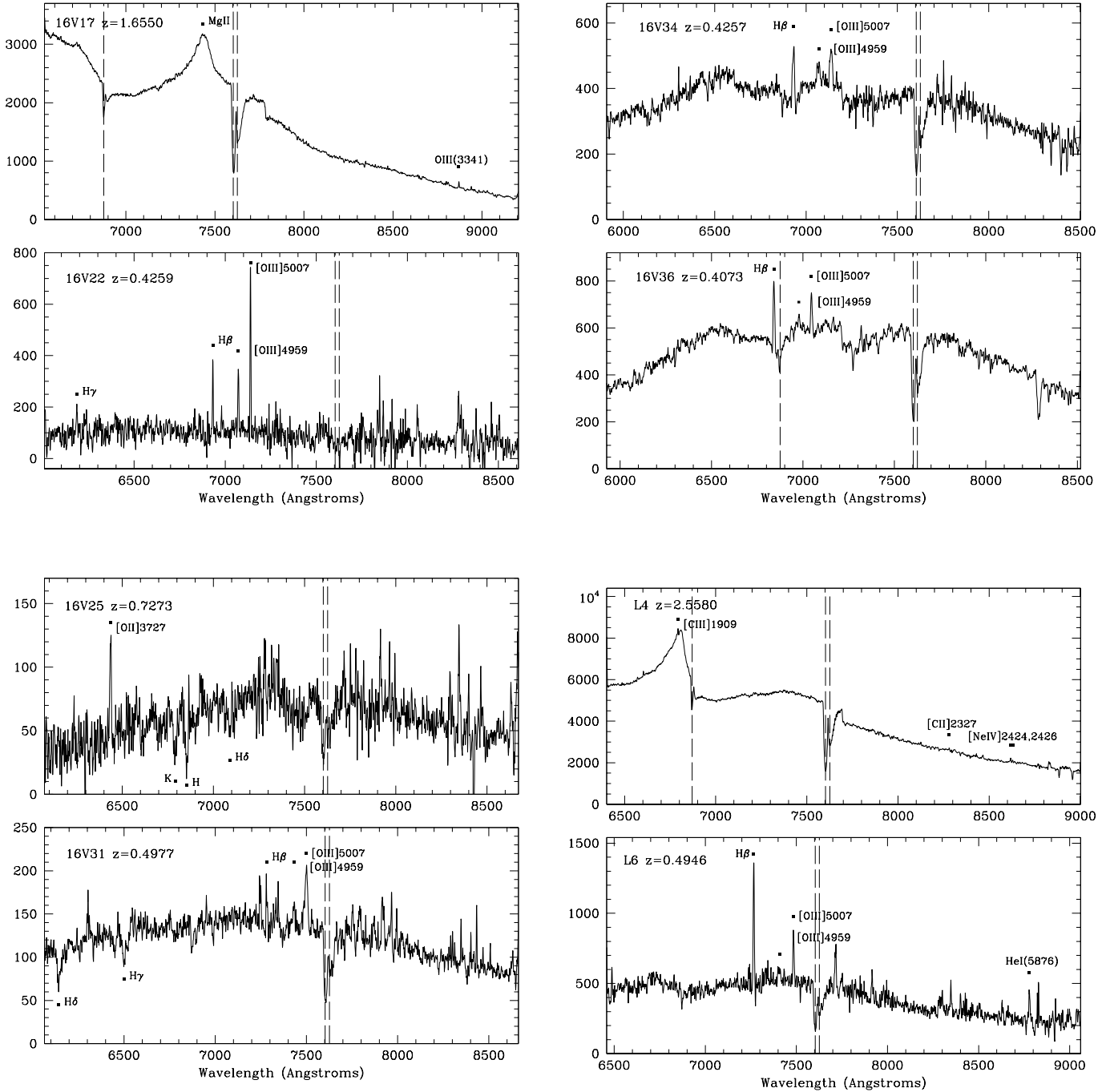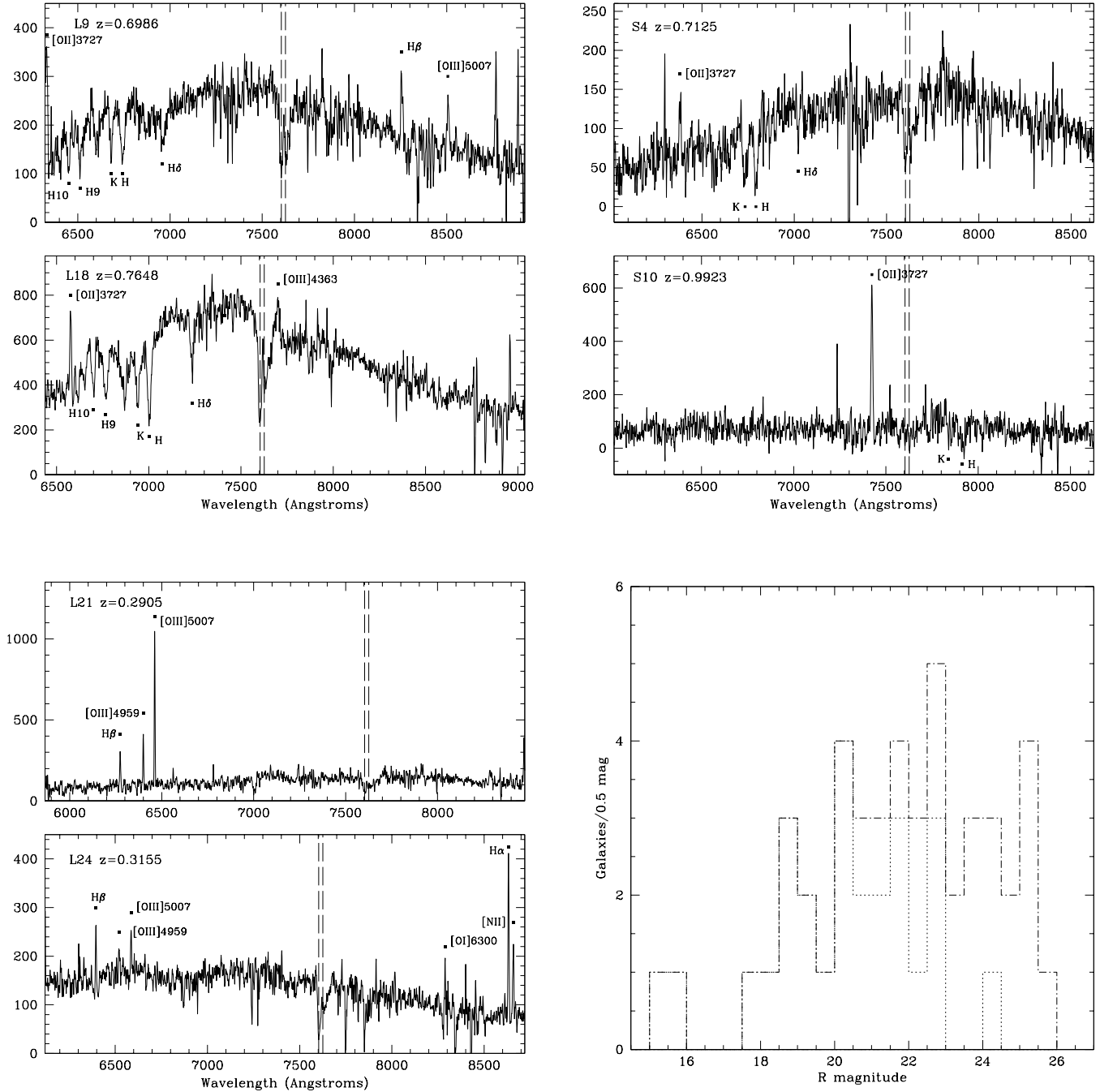
ies, and hence if they are similar types of galaxy they have little ($\Delta(B-R) < 0.5$ mag) or no additional reddening.

The colours of the redshift sample can be interpreted more directly by comparing with a grid of models. We use models (from Roche et al. 2001a) computed with the 'Pegase 2' package (Fioc and Rocca-Volmerange 1997, 1999) to represent normal (non-starburst) spirals from Sa to Im, and E/S0 galaxies. We assume the time-redshift relation of an $\Omega_m = 0.3$, $\Omega_\Lambda = 0.7$, $H_0 = 55$ km s^{-1}Mpc^{-1} Universe, with model galaxies formimg 16 Gyr ago, at $z = 6.05$. The E/S0 galaxies evolve passively (no star-fomation) at $z < 2$. The bluest starburst galaxies are represented as a constant-SFR model observed at an age of 50 Myr, with

no dust reddening, which is redshifted without evolving. The models are computed with a stellar initial mass function (IMF) following the Salpeter slope, $x = 2.35$ where $\frac{dN}{dM} \propto M^{-x}$, at $0.7 < M < 120M_\odot$, but flattening to $x = 1.3$ at $0.1 < M < 0.7M_\odot$ (see Holtzman et al. 1998).

Figure 5 shown the redshift sample on a $B-R$ vs. z plot, on which the majority of the galaxies are close to the spiral models; L3 and 16V22 are significantly bluer suggesting unreddened starbursts, L21, L9, 16V25 and possibly 16V10* are up to 1 mag redder, and the elliptical S5 is consistent with the passive E/S0 models. Figure 6 shows $R-K$ vs. z – again, most of the galaxies are consistent with the spiral

Figure 2. The R magnitude distributions of the radio-source IDs in Table 1 (we have R magnitudes for 47/50) (dashed histogram), and the subset for which we have spectroscopic redshifts (we have R magnitudes for all 26) (bold dotted histogram).

models; L3 and 16V22 are bluer, while 16V25, 16V10*, L9, and also 16V31, are again redder.

6.2 Radio vs. Optical Flux

Condon (1992) models the radio SED of a star-forming galaxy as a summation of thermal ($\nu^{-0.1}$) and synchrotron ($\nu^{-0.8}$) components,

$$F_\nu(\nu) = f_{>5} \, \text{SFR}[5.3 \times 10^{28} \nu^{-0.8} + 5.5 \times 10^{27} \nu^{-0.1}]$$

where F_ν is in ergs s^{-1}Hz^{-1}, ν is frequency in GHz and $f_{>5}$ is the fraction by mass of stars formed with $M > 5 M_\odot$. For the IMF adopted here, $f_{>5} = 0.3095$ (compared to $f_{>5} = 0.1863$

for the standard Salpeter IMF). In Roche et al. (2001a) this relation was used to predict the radio/optical flux ratios for two sets of galaxy models, representing (i) normal, steadily evolving galaxies of Hubble types Sa-Im (colours plotted on Figures 5 and 6), and (ii) starbursting galaxies where a starburst (50 Myr age constant SFR model with $A_V = 0.7$ mag reddening) model SED is added to each normal galaxy, normalized so that the total SFR and hence radio luminosity
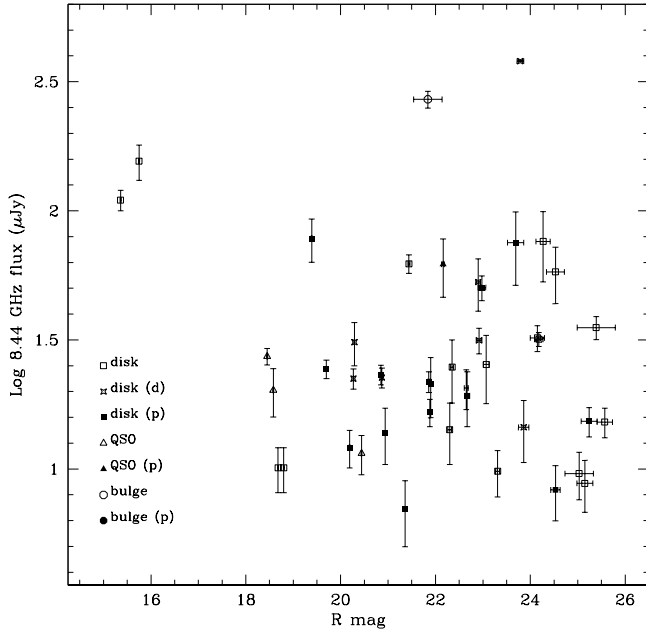
Figure 3. R magnitude against 8.44 GHz flux for 44 radio-selected galaxies (symbol types showing our morphological classifications).
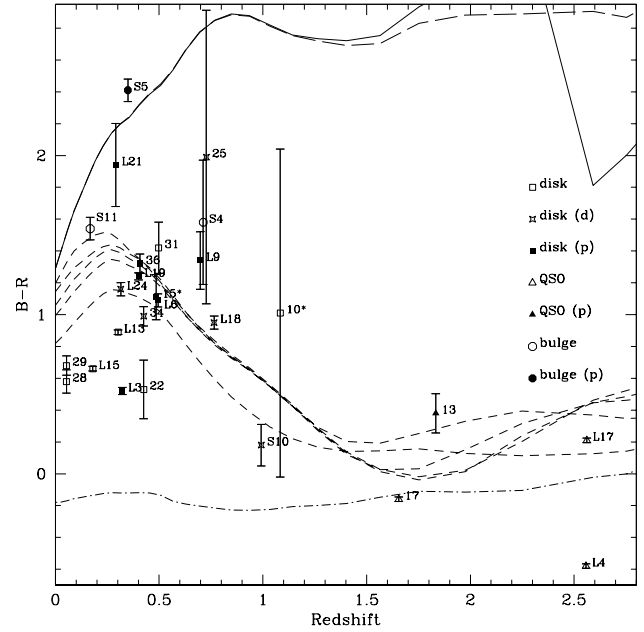

Figure 5. $B - R$ colour (AB system) against redshift for radio-detected galaxies (symbols indicating types), compared to models for evolving spirals – Sa, Sb, Scd, Sc and Im (short-dashed lines, reddest to bluest), early-type galaxies – E (solid) and S0 (long-dashed), and a 50 Myr starburst (dot-dash). The labels of the Lynx2 galaxies omit the '16V' prefix.
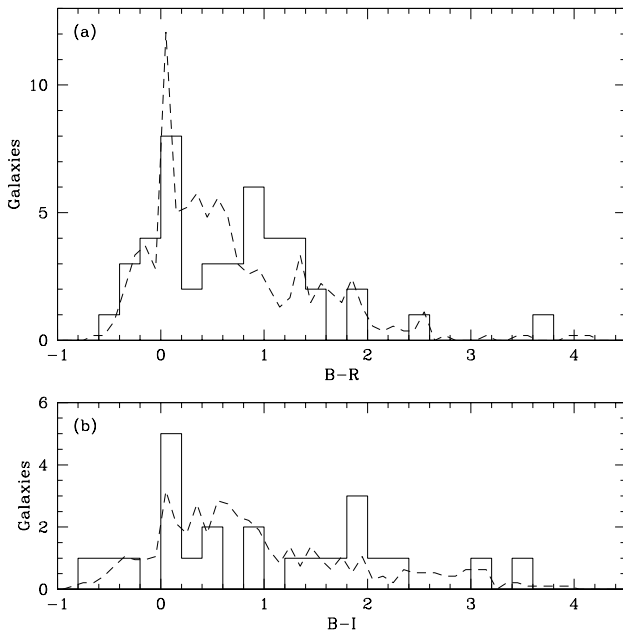
Figure 4. Histograms of (a) the $B-R$ and (b) $B-I$ distributions of the galaxies identified as radio sources, compared with those of all $R < 24.5$ galaxies (dashed line) on the Lynx2 and (for $B-R$) Lilly fields, normalized to the same total number.
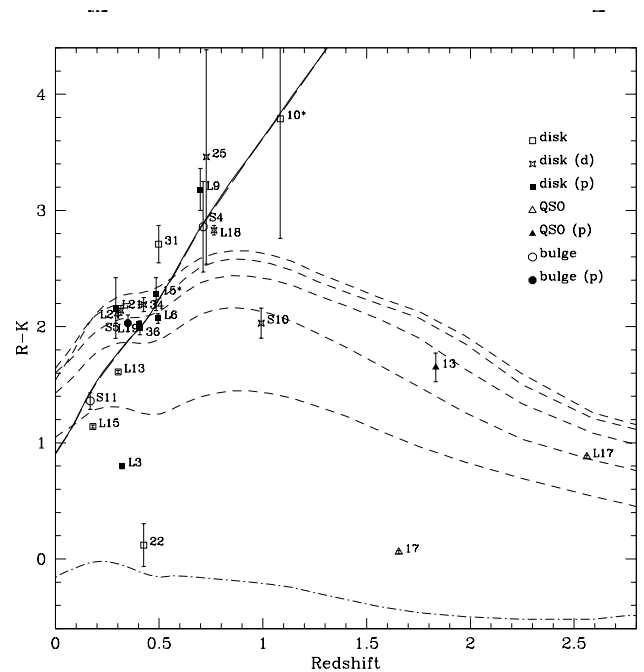
Figure 6. $R - K$ (AB system) against redshift for radio-detected galaxies, with models as Figure 5
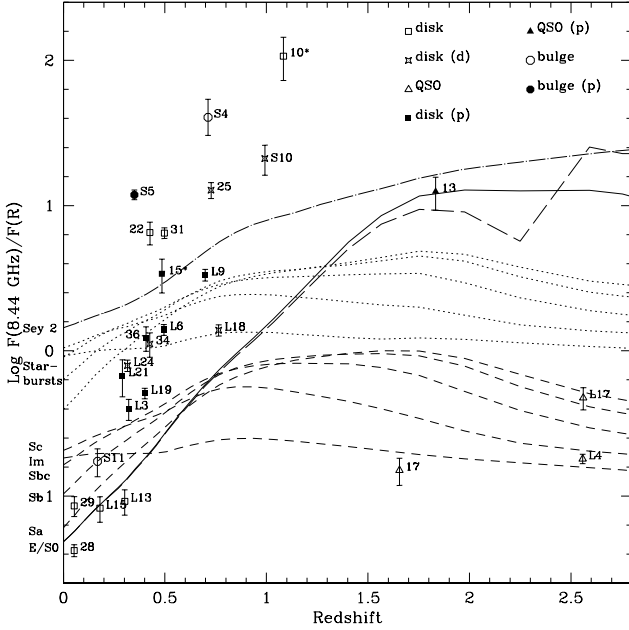
Figure 7. Ratio of 8.44 GHz to R-band flux (F_ν) against redshift, for the radio-detected galaxies, symbols indicating types. These observations are compared with evolving galaxy models for spirals (dashed, models labelled on axis), starburst spirals (dotted, in same order as normal spirals), Seyfert 2 (dot-long dash), and E/S0s (solid/long-dashed) at $M_B = -21.5$.
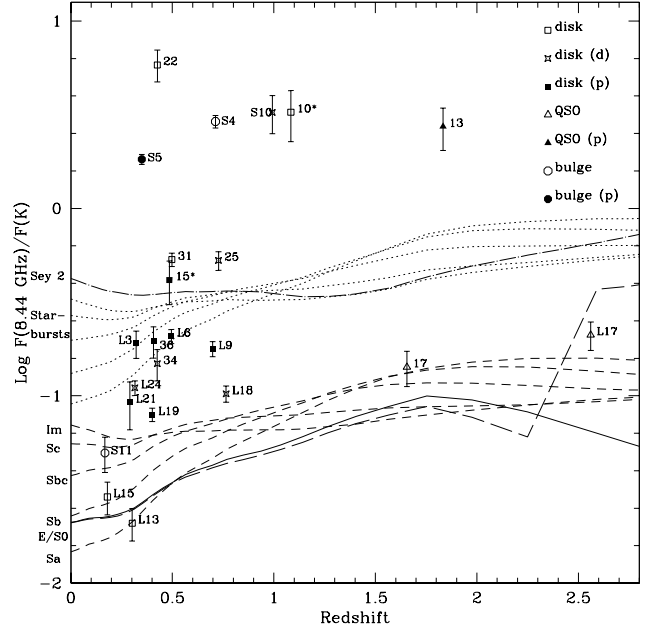

Figure 8. Ratio of 8.44 GHz to K' band flux (F_ν) against redshift, for the radio-detected galaxies observed in K', compared with the same models as plotted in Figure 7.

is increased by ~ 0.8 dex. For E/S0 galaxies we adopted an observational radio/optical ratio, from the $L_{rad} \propto L_B^{2.2}$ relation of Sadler, Jenkins and Kotanyi (1989).

Figure 7 shows the 8.44 GHz to R-band flux ratio vs. redshift, compared with the Roche et al. (2001a) models for normal and starburst galaxies. The elliptical flux ratio is plotted for $M_B = -21.5$, and will be 0.48 dex higher for each 1 mag brighter in optical luminosity. Also shown is a model for Seyfert 2s based on the tabulated mean SED of Schmitt et al. (1997). Figure 8 shows the same for the 8.44 GHz to K' ratio. Both figures show that: (i) four $z < 0.4$ disk galaxies and the elliptical S11 have relatively low ratios of radio to R or K' flux, consistent with normal non-starburst spirals and ellipticals; (ii) three of the QSOs have similar low ratios but 16V13 is an order of magnitude higher; (iii) most radio IDs have ratios in the range of our starburst models, but (iv) seven (16V10*, 22, 25, 13, S4, S5 and S10) are significantly higher – implying extreme SFRs, greater dust extinction, and/or radio-loud AGN.

6.3 Radio and Optical Luminosity

Radio luminosities and B and K' absolute magnitudes are estimated from the observed fluxes and magnitudes as described in Appendix 1. For S5 and S11, we make use of B and R magnitudes derived from Munn et al. (1997) (Table 1) in deriving the M_B and M_K, but for S4 use only our own I and K' photometry (I being close to rest-frame B at this redshift).

Concerning the radio luminosities, note that:

Table 3. Estimated absolute magnitudes M_B and M_K in rest frame B and K' respectively, and 8.44 GHz restframe radio luminosities $L_{8.44}$ for the 26 galaxies in the redshift sample.

Source	M_B	M_K	$\log L_{8.44}$	Redshift
16V10*	-22.37	-24.69	40.76	1.0838
16V13	-25.61	-26.18	41.17	1.8330
16V15*	-21.02	-23.40	39.43	0.4854
16V17	-27.36	-27.50	40.59	1.6550
16V22	-19.87	-19.86	39.29	0.4259
16V25	-22.08	-24.71	39.99	0.7273
16V27	[1]	-30.69	42.36	1.680
16V28	-21.71	$-23.56^{[1]}$	38.08	0.0531
16V29	-21.28	$-23.09^{[1]}$	38.23	0.0535
16V31	-21.65	-24.37	39.92	0.4977
16V34	-22.19	-24.53	39.47	0.4257
16V36	-22.91	-25.08	39.82	0.4073
L3	-21.51	-22.28	38.79	0.322
L4	-28.57	$-28.23^{[1]}$	41.11	2.5580
L6	-22.14	-23.78	39.44	0.4946
L9	-22.77	-25.15	39.80	0.6986
L13	-22.67	-24.38	38.65	0.302
L15	-21.42	-22.75	38.16	0.180
L17	-27.50	-27.63	40.73	2.561
L18	-24.00	-26.17	39.90	0.7648
L19	-22.57	-24.76	39.91	0.401
L21	-19.77	-22.31	38.45	0.2905
L24	-21.28	-23.63	39.04	0.3155
S4	-22.56	-25.15	40.91	0.7125
S5	$-22.52^{[2]}$	$-24.68^{[2]}$	40.71	0.3493
S10	-22.47	-24.01	40.54	0.9923
S11	$-21.79^{[2}$	$-23.70^{[2]}$	38.80	0.168

[1] Not observed in K'. M_K is estimated by extrapolating the model SED fitted to the observed $B - R$. [2] Munn et al. (1997) B and R mags (Table 1) used in estimate.

(i) The radio k-corrections (Appendix 1) are dependent on the assumed Condon (1992) SED, in which the thermal ($\nu^{-0.1}$) component is 0.34 of the total flux at 10 GHz. This fraction is consistent with the mean of 0.30 ± 0.05 for spirals in the Shapley-Ames catalog (Niklas, Klein and Wielebinski 1997), but the thermal fraction is > 0.45 in 15 per cent of these galaxies, and in the top 6 per cent reaches 0.60–0.75. If a galaxy at $z = 0.75$ has a thermal-component fraction of 0.68 at 10 GHz, our rest-frame $L_{8.44}$ would be an overestimate by 0.06 dex.

(ii) Carilli (2000) predicts a radio luminosity per unit SFR 2.35 times higher than Condon (1992), on the basis of the observed radio/FIR flux ratio and FIR emission from a model starburst. This estimate was based on the extreme assumption that the fraction of the bolometric emission going into dust emission is unity, which may be approximately valid for dusty starbursts, but in our models for normal spirals this fraction is only ~ 50 per cent, which would reduce the radio flux per unit SFR almost to the Condon (1992) value. We consider both models, as it seems likely that real L_{rad}/SFR ratios would lie in the range between the two, perhaps depending on the type of galaxy.

Figure 9 shows the radio/optical luminosity ratio, in the form of the restframe flux ratio,

$\log [F_\nu(8.44)/F_\nu(B)] = \log L_{8.44} - \log (8.44 \times 10^9) - [40.08 - 23.0 + \log 3631 - 0.4 M_B]$
$= \log L_{8.44} - 30.566 - 0.4 M_B$

against M_B. These ratios are compared with (i) our Im model (approximately constant-SFR) at $z = 0$ (ii) the same model with the additional starburst component, increasing the total SFR by a factor 8. Figure 10 shows the ratio $\log (F_\nu(8.44)/F_\nu(K'))$ against M_K; this, as the K'-band will be less sensitive to starbursts and dust than B, should give a more direct indication of the SFR per unit stellar mass. We find that the redshift sample consists of galaxies with a very wide, ~ 2.5 order of magnitude, range of radio/optical ratios, indicating a diverse mix of normal galaxies, moderate and extreme starbursts, and AGN.

7   INTERACTING PAIRS

We identify 10 close pairs within the redshift sample. With our chosen detection criteria, 8 of these pairs were detected as separate galaxies on both the LRIS and K' image and the radio source is assumed to be the component with the lowest value of P (Section 4.1), hereafter the 'primary'. 16V36 and L21 were detected as single sources on the LRIS image but are visibly double nucleus systems, and detected as pairs on the higher resolution NIRC images (the K' magnitudes in Table 1 are for the two components combined).

16V36 shows prominent tidal tails, confirming it is a merger. The two components of 16V15* are verified by spectroscopy to be at almost identical redshifts, as have the two bright galaxies 16V28/9. In the case of the other pairs a firm confirmation of interaction may require further (e.g. WFPC2 or STIS) data. However, the statistical significance of their close pairing can be estimated by calculating a pair probability Pp, again using the formula

$$Pp = 1.0 - \exp(-\pi r^2 n(m))$$

where r is the separation of the two nuclei (as fitted with
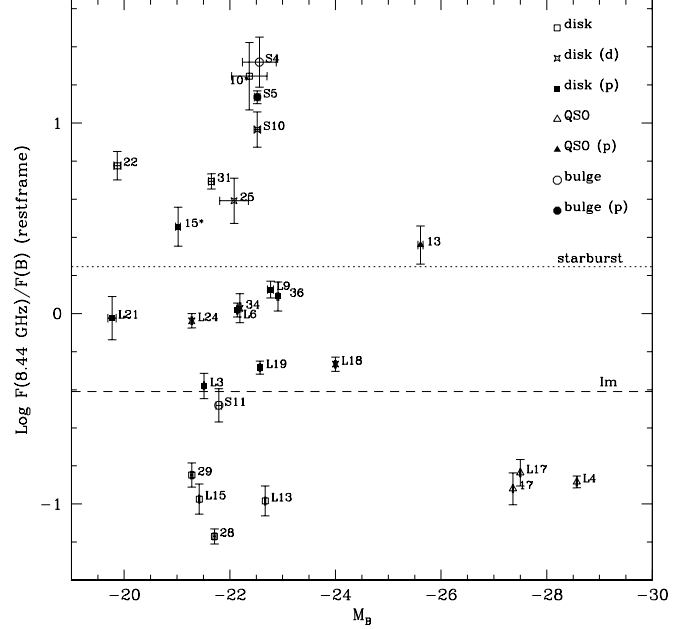
Figure 9. Ratio of rest-frame 8.44 GHz to B-band flux against B absolute magnitude, for radio-detected galaxies. The dashed line shows the flux ratio of the Im model at $z = 0$; the dotted line the Im model with the addition of a starburst, increasing the SFR by factor 8.
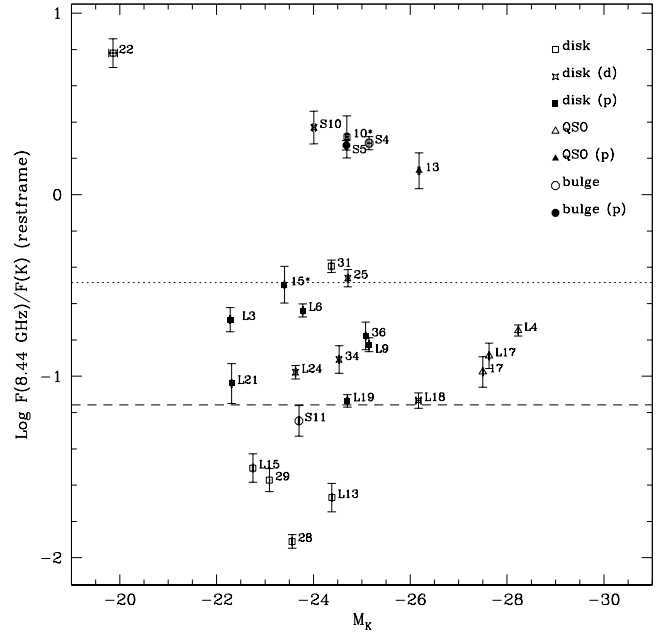
Figure 10. Ratio of rest-frame 8.44 GHz to K'-band flux against K' absolute magnitude. Models as in Figure 9.

Table 4. Close (likely merging/interacting) pairs of galaxies in the sample of radio detection with redshifts: projected separation r, observed flux ratio of secondary to primary (assumed radio source) galaxy (in the R-band unless otherwise stated) and estimated probability Pp of the pair occurring by chance.

Source	Pair separation		R flux ratio	Pp
	arcsec	h_{50}^{-1} kpc		
16V13 (B)	4.94	58.4	0.116	0.211
16V13 (C)	4.84	57.2	0.145	0.213
16V13 (D)	4.13	48.8	0.086	0.223
16V15*	2.50	21.1	1.117	0.004
16V28/9	65.1	94.9	0.698	0.023
16V36	1.84	14.0	0.912[1]	0.001
L3	6.57	43.1	0.205	0.041
L6	3.05	26.0	0.347	0.013
L9	4.47	44.8	0.429	0.064
L19	2.58	19.5	0.395	0.004
L21	2.83	17.3	0.310[1]	0.030
S5	6.06	42.0	0.052[1]	0.018

[1] K' flux ratio

SExtractor), $n(m)$ the integral number count (surface density) of galaxies brighter than the secondary (fainter) galaxy of the pair (magnitude m). Pp is then the probability that a companion galaxy of similar or greater brightness would, entirely by chance, lie at a similar or closer distance from the galaxy identified as the radio source.

Table 4 gives the separations of the galaxies, r, in arcsec and in h_{50}^{-1}kpc, and the R flux ratio (primary/secondary). 16V13 has three companions detected as separate objects on the LRIS image, and parameters are given for each ('B', 'C' and 'D'). Excluding 16V13, the probability of each of these pairs being a chance coincidence is < 7 per cent. In the case of 16V13, the companion galaxies are faint and there is over a 20 per cent probability of each being a chance coincidence, but the likelihood of all three would be ~ 1 per cent.

The mean luminosity ratio of these pairs is 0.40 ± 0.11, and the mean projected separation $41 \pm 7~h_{50}^{-1}$ kpc, reducing to 36 ± 5 if the wide 16V28/9 pair (which are not obviously interacting) is excluded. This mean separation is similar to that of both interacting FRII radio galaxies (Roche and Eales 2000b) and of local radio-selected starbursts (Smith, Herter and Haynes 1998), but greater (although marginally) than the $19.1 \pm 2.1~h_{50}$ kpc estimated for merging ULIRGs (Clements et al. 1996).

8 SPECTRAL LINE EQUIVALENT WIDTHS

8.1 Hγ and Hδ

Delgado, Leitherer and Heckman (1999) model Balmer line EWs in starburst and post-starburst galaxies. Star-forming nebulae produce Hβ, Hγ and Hδ emission (with Hβ the strongest) and stars (especially spectral type A) absorb these lines, so the observed EWs are the difference $EW_{em} - EW_{abs}$. During the burst the emission dominates, but if star-formation is halted it rapidly declines to zero (within ~ 15 Myr), and absorption becomes dominant, peaking ($EW_{abs} \sim 13$Å) after ~ 500 Myr. Figure 11 shows a Delgado et al. (1999) model for an instantaneous, solar-metallicity
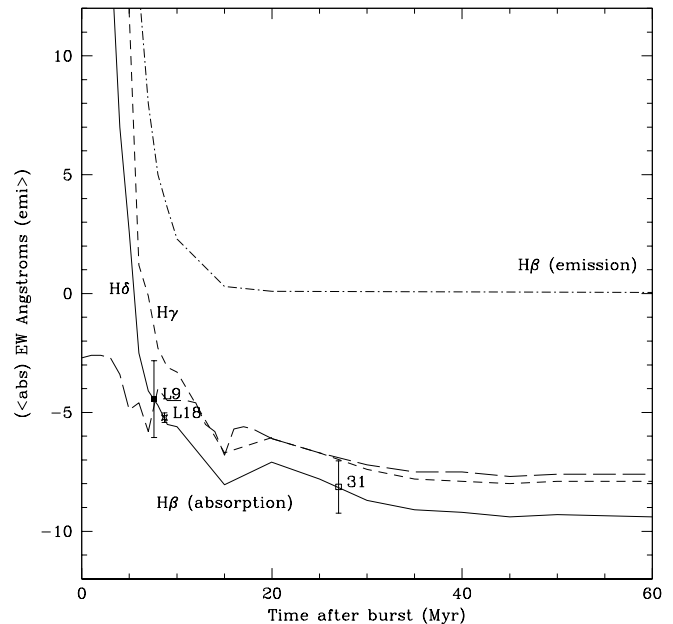
Figure 11. Delgado et al. (1999) model for the post-starburst evolution of Balmer lines (emission positive, absorption negative), showing the total (emission-absorption) EWs for Hγ (short-dash) and Hδ (solid line) and for Hβ the emission (dot-dash) and absorption (long-dash) EWs separately. The plotted points are the Hδ EWs of the three 'e(a)' galaxies, at the starburst ages best fitting the model.

burst – for Hβ we plot the emission and absorption components separately, and show total EWs for Hγ and Hδ. In a constant-SFR model (Delgado et al. 1999), Hδ is seen in emission for the first ~ 100 Myr. If steady star-formation continues Gyr, i.e. as in normal spirals, it becomes an absorption line, but remains weak compared to that in post-starbursts.

Poggianti and Wu (2000) define a class of 'e(a)' galaxies, with both strong Balmer absorption, EW(Hδ) > 4Å, and some moderate emission in, e.g., [OII]3727Å. Galaxies with e(a) spectra may be post-starburst galaxies with some residual, ongoing star-formation. However, Poggianti, Bressan and Franceschini (2000) find that e(a) spectra can also be produced by active starburst galaxies if the most recently formed stars are hidden by dust ('age-dependent extinction') (Section 10.3)

All non-QSO galaxies in our redshift sample show Hβ and/or [OII]3727Å emission. Hγ is seen in absorption for 16V31 and emission for 16V22 and 16V15*, but in other galaxies is consistent with zero. Hδ is seen in absorption in 16V25, 16V31, L9, L18 and S4, but is possibly a weak emission line in 16V10*. These emission lines indicate that 16V15*, 16V22 and 16V10*, at least, are actively starbursting. For 16V25 and S4, EW(Hδ) < 4Å, which is consistent with normal spirals. The larger EW(Hδ) of 16V31 (8.14 ± 1.10Å), L9 (4.44 ± 1.61Å) and L18 (5.22 ± 0.20Å) classifies these as e(a) galaxies, and, if interpreted in terms of a simple post-starburst model (Figure 12) corresponds to respective intervals 27 Myr, 7.6 and 8.7 Myr after the truncation of star-formation.

Table 5. Stellar-absorption corrected Hβ EW, log Hβ luminosity, and SFR estimates from Hβ and 8.44 GHz luminosities. SFR(8.44) is given for the Condon (1992) relation and is lower by a factor of 2.35 for the Carilli (2000) model.

Galaxy	EW(H$_\beta$)$_{corr}$ Å	log L(Hβ) ergs s^{-1}	SFR(Hβ) $M_\odot$yr^{-1}	SFR(8.44)
16V15	12.29 ± 0.36	41.30	3.87	74.1
16V22	11.62 ± 0.34	40.77	1.14	53.7
16V31	9.99 ± 0.60	41.53	6.57	229.
16V34	7.24 ± 0.24	41.52	7.71	81.3
16V36	7.52 ± 0.17	41.86	14.1	182.
L6	10.53 ± 0.22	41.68	9.22	75.9
L9	13.33 ± 0.48	42.12	25.3	174.
L21	15.00 ± 0.56	41.02	2.05	7.76
L24	6.75 ± 0.31	41.14	2.68	30.2

8.2 Hβ

We observe Hβ emission for 9 galaxies. The luminosity, L(Hβ), is a good tracer of the SFR on very short timescales - it takes only ~ 8 Myr to fall by two orders of magnitude if star-formation ceases (Delgado et al. 1999). However, the observed Hβ) flux is affected by both dust extinction and the superimposed absorption of the stars; the latter reduces the EW by ~ 2–5Å in normal spirals (Guzmán et al. 1998).

Kennicutt (1983) derived a relation L(Hα) $= 7.02 \times 10^{41}$ SFR(> 10M$_\odot$) ergs s^{-1}, in the absence of dust Hα $= 2.86$Hβ (Guzmán et al. 1997), and for our assumed IMF the mass fraction of $M > 10M_\odot$ stars is 0.2105 (0.1267 for the Salpeter IMF). Combining these gives L(Hβ) $= 5.17 \times 10^{40}$ SFR ergs s^{-1} (where the SFR is for all masses).

To estimate L(Hβ) we first estimate an AB absolute magnitude for the 4861Å continuum, M_{4861}, using the observed B and R magnitudes (as in Appendix 1). A correction for stellar absorption is added to all the observed EW(Hβ), to give EW(Hβ)$_{corr}$. The stellar absorption is assumed to be 2.7Å – the mean for $z < 0.7$ star-forming galaxies in the Canada-France Redshift Survey (Hammer et al. 1997) – for all except the e(a) galaxies, for which we estimate 6.90Å for 16V31 and 4.72Å for L9, from the Delgado et al. (1999) post-starburst models best fitting their EW(Hδ). The line luminosity is then
L(Hβ) $= 10^{40.08} \times 10^{-19.44-0.4M_{4861}} \times c/\lambda^2 \times$ EW(Hβ)$_{corr}$ ergs s^{-1},
log L(Hβ) $= 20.64 - 0.4$M$_{4861}$ + log(1.2686×10^{11}) + log EW(Hβ)$_{corr}$

(Table 5). Also given are the $H\beta$ and radio (Condon 1992) SFR estimators, L(Hβ)/(5.17×10^{40}) and $L_{8.44}/(3.66 \times 10^{37})$ (both scale with H_0 as h_{50}^{-2}). The Carilli (2000) model with our IMF gives a lower SFR of $L_{8.44}/(8.60 \times 10^{37})$, which can be regarded as a lower limit. With the standard Salpeter IMF, the SFR estimators increase by factors of 1.66 with no change in their ratio. Combining these models (with no dust extinction) predicts log L(Hβ) $=$ log $L_{8.44} + k$ where $k = 2.78$ (Carilli 2000) to $k = 3.15$ (Condon 1992). Figure 11 shows L(Hβ) against $L_{8.44}$. The two luminosities are correlated (correlation coefficient 0.71), with a best-fit power-law log L(Hβ) $= 15.73 + 0.652$log $L_{8.44}$, and a scatter σ(log L(Hβ)) $= 0.30$. In all 9 galaxies, the L(Hβ)/L$_{8.44}$ ratio is lower – typically by an order of magnitude – than the models. At the mean log $L_{8.44}$ of 39.41, Hβ
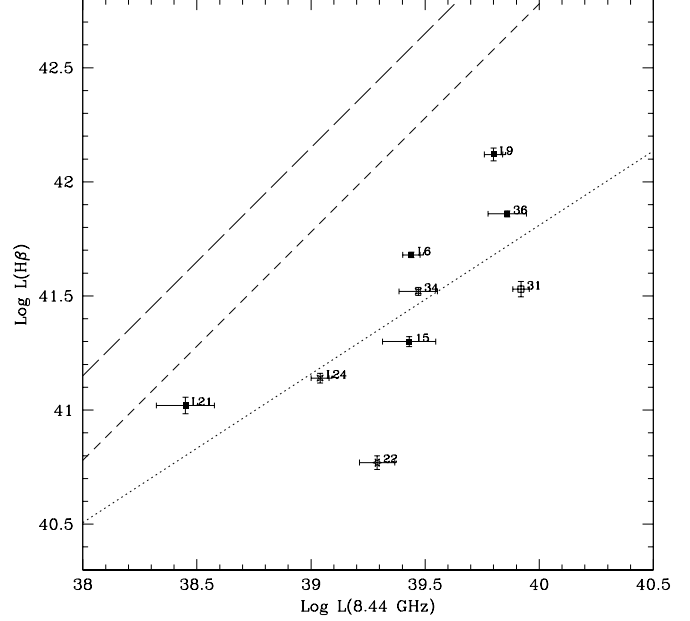
Figure 12. Log L(Hβ) against $L_{8.44}$ in h_{50}^{-1} ergs s^{-1} for the 9 radio-detected galaxies with EW(Hβ). The short-dashed and long-dashed lines show the Carilli (2000) and Condon (1992) relations, with the assumption of no dust extinction, and the dotted line the power-law best-fitting the data.

is $2.5(39.41 + k - 41.43) = 1.9$–$2.8 \pm 0.25$ mag fainter than predicted. We discuss this further in Section 10.5.

8.3 [OII] 3727Å

The [OII] 3727Å emission line is also an indicator of the current SFR – Kennicutt (1992) estimates L([OII]) $= 3.15 \times 10^{41}$ SFR(> 10M$_\odot$) ergs s^{-1} (with no dust). For the IMF adopted here, this becomes L([OII]) $= 6.63 \times 10^{40}$ SFR ergs s^{-1}.

We detected [OII] emission from 6 of the galaxies. Estimating continuum absolute magnitudes at 3727Å, M_{3727}, by the same method as used above for M_{4861}, the luminosity
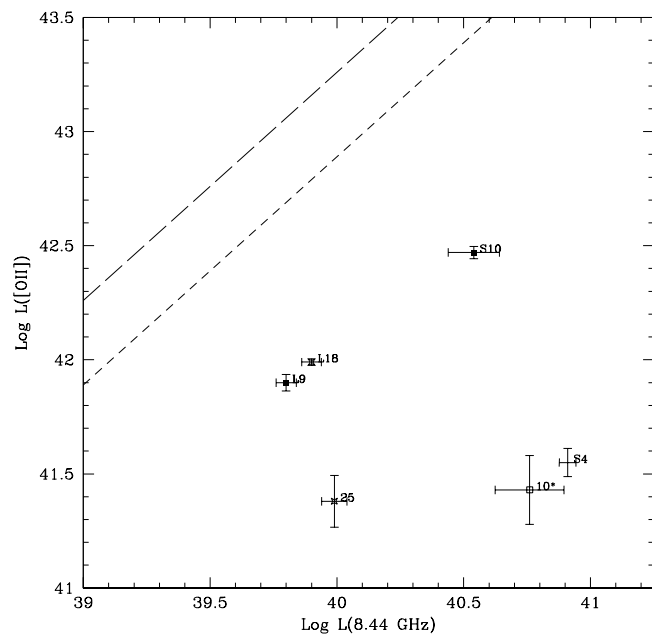L([OII]) $= 10^{40.08} \times 10^{-19.44-0.4M_{3727}} \times$ c/$\lambda^2 \times$ EW([OII]) ergs s^{-1},
log L([OII]) $= 20.64 - 0.4$M$_{3727}$ + log(2.158×10^{11}) + log EW([OII])

is given in Table 6, with the SFR as estimated from L([OII]) and $L_{8.44}$. S10 has a high EW([OII]), typical of a late-type starburst, while the the other 5 have moderate EWs in the range of normal Sb–Sc spirals (Kennicutt 1992; Sodre and Stasinska 1999). Figure 12 shows L([OII]) against $L_{8.44}$, together with the no-dust models, log L([OII]) $=$ log $L_{8.44} + k$ with $k = 2.89$ (Carilli 2000) and $k = 3.26$ (Condon 1992). With so few points the luminosities are not significantly correlated, but the mean log L([OII]) $-$ log $L_{8.44}$ is 1.47 (with scatter 0.68), corresponding to $2.5(k - 1.47) = 3.6$–4.5 ± 0.7 mag extinction at 3727Å. If 16V10* and S4 are excluded (on the grounds that they may have obscured AGN) the mean log ratio is 1.90 (scatter 0.34), indicating 2.49–3.4 ± 0.7 mag.

Table 6. [OII]3727Å EW (in Å), log [OII] luminosity (ergs s^{-1}), and SFR estimates (in $M_\odot$yr^{-1}) from [OII] and 8.44 GHz luminosities, for galaxies with detected [OII] emission. SFR(8.44) is given for the Condon (1992) relation and is lower by a factor of 2.35 for the Carilli (2000) model.

Galaxy	EW([OII])	log L([OII])	SFR([OII])	SFR(8.44)
16V10*	7.37 ± 1.10	41.43	4.06	1585.
16V25	8.78 ± 0.56	41.38	3.67	269.
L9	15.45 ± 0.98	41.90	11.9	174.
L18	5.68 ± 0.15	41.99	14.7	219.
S4	7.54 ± 0.53	41.55	5.32	2239.
S10	52.50 ± 0.84	42.47	44.6	955.

Table 7. EW([OIII]5007) (in Å) and the ratio of [OIII] to absorption-corrected $H\beta$ flux (excitation), for galaxies observed at O[III].

Galaxy	EW([OIII])	F([OIII])$/F$(Hβ)
16V15	6.16 ± 0.37	0.576 ± 0.051
16V22	30.19 ± 0.54	2.925 ± 0.138
16V31	6.29 ± 0.44	0.683 ± 0.091
16V34	3.37 ± 0.27	0.536 ± 0.061
16V36	2.28 ± 0.08	0.325 ± 0.019
L6	3.81 ± 0.21	0.418 ± 0.032
L9	6.74 ± 0.54	0.542 ± 0.064
L21	40.19 ± 0.66	2.744 ± 0.148
L24	2.70 ± 0.31	0.461 ± 0.074

Figure 13. Log L([OII]3727Å) against $L_{8.44}$, in h_{50}^{-1} ergs s^{-1}, for the 6 radio-detected galaxies with EW([OII]). The short-dashed and long-dashed lines show the Carilli (2000) and Condon (1992) relations, with the assumption of no dust extinction.

8.4   [OIII] 5007Å

The ratio of [OIII]5007Å to Hβ flux ('excitation') is a useful diagnostic of the type of galaxy. In local galaxies, it typically increases from ~ 0.2 to 1–2 from Sb to Im types (Sodre and Stasinska 1999), and further to a mean of 3.1 ± 0.3 for dwarf HII galaxies (Guzmán et al. 1997). The excitation of starburst galaxies may cover a wide range from ~ 0.3 to ~ 5.0 (Tresse et al. 1996), and is strongly dependent on metallicity; models predict it to increase slightly from $0.1Z_\odot$ to a peak at $0.25Z_\odot$, then fall by factors 2–3 to $1Z_\odot$ and by a further order of magnitude to $2Z_\odot$. Higher excitations of ~ 5–15 are observed in Seyferts and are usually interpreted as evidence for an AGN.

[OIII] emission was observed for the same 9 galaxies as Hβ. As described in Appendix 1, we estimate from the colours of each, the ratio of the continuum F_ν at 5007Å to that at 4861Å, typically ~ 1.1. This ratio is multiplied by EW([OIII])/EW(Hβ)$_{corr}$ (Table 5), giving the excitation (Table 7).

These excitations are bimodally distributed, with 7/9 galaxies forming a group with a mean of 0.51 and a small scatter of 0.12, while 16V22 and L21 both have high excitations of ~ 2.8. None have excitations sufficiently high to require an AGN contribution. The excitation is negatively correlated with B luminosity (correlation coefficient 0.88). 16V22 and L21 are optically the least luminous galaxies in the redshift sample, with $M_B > -20$. Their M_B, L(Hβ) and excitations are similar to those of the $z < 0.7$, low metallicity($\sim 0.4Z_\odot$) HII galaxies studied by Guzmán et al. (1997). The excitations of the other 7 are in the lower half of the range of more luminous ($L \sim L^*$), metal-rich ($Z_{mean} \sim 0.8$–$1Z_\odot$) starburst and interacting spirals (Gallego et al. 1997; Pastoriza and Donzelli 2000).

Kobulnicky and Koo (2000) describe an estimator of metallicity (O/H), originally from McGaugh (1991), based on the ratio of emission line fluxes $R_{23} = (\frac{\text{[OII]}3727 + \text{[OIII]}4959 + \text{[OIII]}5007}{\text{H}\beta})$. Assuming [OIII]4959 = [OIII]5007/2.9 and the [OII] to [OIII] relation fitted to HII galaxies by McCall, Rybski and Shields (1985), the ~ 2.8 excitation of 1622 and L21 corresponds to log $R_{23} \simeq 0.825$ and $\log(Z/Z_\odot) \simeq -0.25$ and the 0.51 ± 0.12 of the more luminous galaxies to log $R_{23} \simeq 0.45 \pm 0.05$ and $\log(Z/Z_\odot) \simeq +0.05 \pm 0.03$. The excitation/metallicity vs. luminosity trend of these 9 galaxies ($z_{mean} = 0.45$) appears consistent with that seen for the $z \sim 0$–0.4 emission-line galaxies of Kobulnicky and Koo (2000).

9   KINEMATICS FROM EMISSION LINES

The 2D profiles of spectral emission lines may provide information on the galaxy kinematics – internal velocity dispersion and rotation velocity. These can distinguish between giant spirals (high dispersion and rotation), normal giant ellipticals (high dispersion, low or zero rotation), and dwarf galaxies (low dispersion, low or zero rotation), and furthermore the rotation velocity of spirals is well correlated with mass and optical luminosity.

9.1   Velocity Dispersion

In many of our spectra the emission lines are noticeably broader than the instrumental resolution. Guzmán et al.

Table 8. Internal velocity dispersion σ_i and the shift in velocity across the galaxy Δv, as estimated from the profiles of the strongest emission lines.

Galaxy	σ_i (km s^{-1})	Δv (km s^{-1})
16V10	177 ± 28	202 ± 67
16V15	90 ± 5	40 ± 17
16V22	58 ± 2	15 ± 7
16V25	151 ± 11	164 ± 36
16V31	260 ± 23	333 ± 81
16V34	225 ± 16	450 ± 37
16V36	166 ± 6	71 ± 38
L6	88 ± 3	149 ± 28
L9	199 ± 12	344 ± 22
L18	163 ± 5	198 ± 17
L21	47 ± 2	21 ± 9
L24	87 ± 14	7 ± 26
S4	211 ± 18	311 ± 59
S10	160 ± 3	216 ± 12

(1997), observing faint compact galaxies with the same spectrograph, estimated internal velocity dispersions (σ_i) as

$$\sigma_i = \sqrt{(\mathrm{FWHM}^2 - (3.1\text{Å})^2)} \times \frac{c}{2.35\lambda_0(1+z)}$$

where σ_i is the rest-frame internal velocity dispersion of the galaxy, the line FWHM is from a Gaussian fit to the strongest emission line in the spectrum, λ_0 is the restframe wavelength of this line, and 3.1Å is the effective instrumental resolution of LRIS with the 600 mm^{-1} grating.

Applying this method to our spectra, using in most cases the H_β line, we find a significantly positive σ_i for all 14 non-QSO galaxies (Table 8).

We find σ_i to be correlated (correlation coefficient 0.75) with luminosity (Figure 13); the best-fitting power-law is $\log \sigma_i = -0.1506 M_B - 1.181$, with a scatter $\sigma(\log \sigma_i) = 0.15$. If these are disk galaxies, σ_i will be related to the rotation velocity (on the flat outer part of the rotation curve) v_{rot}, although with a large scatter due to the random orientations.

Using simulations Rix et al. (1997) predict most spirals in a randomly oriented sample will have $\sigma_i/v_{rot} = 0.45$–0.9, with an average $\sigma_i/v_{rot} \simeq 0.65$. Rubin et al. (1985) give observed v_{rot}–M_B relations for Sa, Sb and Sc spirals (plotted on Figure 13). If our galaxies are like local spirals, they would, due to their random orientations, lie an average of ~ 0.19 dex below these relations. In addition, galaxy evolution is reported to shift the local v_{rot}–M_B relation by up to $\Delta(M_B) \sim -0.6$ mag at these redshifts (Vogt et al. 1996), equivalent to $\Delta(v_{rot}) = -0.06$ dex at a given M_B. Hence, for a direct comparison with our σ_i, we also plot the Rubin et al. (1985) relations shifted down by $\Delta(v_{rot}) = -0.25$ dex. Also shown is the Telles and Terlevich (1993) σ_i–M_B for HII galaxies, which have much lower internal velocities than spirals of the same M_B (see also Koo et al. 1995).

We find that the more luminous ($M_B < -21.5$) galaxies generally have σ_i consistent with the relations for spirals, but the low-luminosity 16V22 and L21 have σ_i below these relations and may be more consistent with HII galaxies.
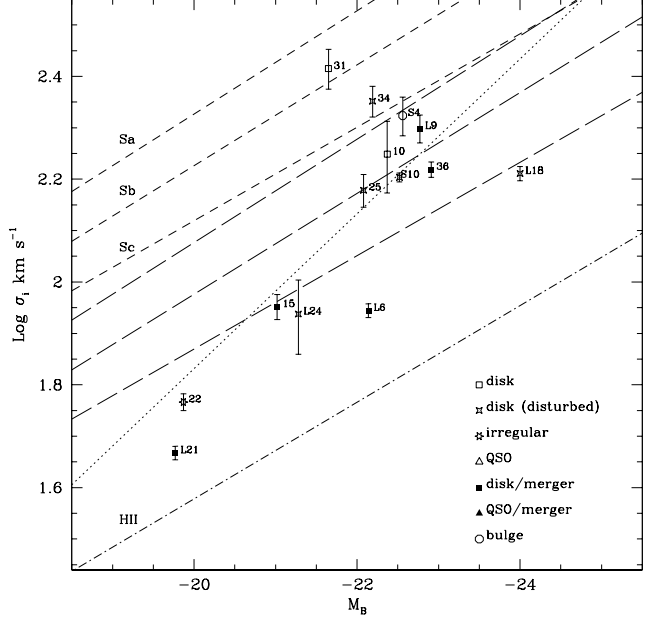

Figure 14. Internal velocity dispersion (σ_i), as estimated from emission-line FWHM, against blue absolute magnitude M_B. The dotted line is the power-law best fitting these data. The short-dashed lines show the mean relations of rotation velocity (not σ_i) to M_B for Sa, Sb and Sc spirals, from Rubin et al. (1985). The long-dashed lines show these same relations shifted downwards by 0.25 dex to more directly compare with the observed σ_i (see text). The lowest, dot-dash line is the Telles and Terlevich (1993) σ_i–M_B relation for HII galaxies.

9.2 Rotation Velocity

A second and more direct measure of galaxy kinematics is the shift in an emission line's centroid wavelength across the galaxy in the spatial direction. The wavelength shift $\Delta\lambda$ corresponds to a rest-frame radial velocity, $\Delta v = \frac{c\Delta\lambda}{\lambda_0(1+z)}$. An edge-on spiral with long axis along the spectroscopic slit will approach $\Delta v \sim 2v_{rot}$, but a sample of randomly oriented spirals will be closer to $\Delta v \sim v_{rot}$, with a large scatter.

On our 2D (spectral $x \times$ spatial y) spectra, the majority of the galaxies show diagonally slanted emission lines. From each 2D spectrum, we extract a series of 5–8 1D spectra from narrow strips of width $\Delta y = 4$ pixels, shifting the strip aperture in steps of $\Delta y = 2$ pixels across the visible width of the spectrum, and then for each of these narrow-strip spectra measure (with a Gaussian fit) the centroid wavelength of the strongest emission line. Figure 15 shows, for four of the more strongly rotating galaxies, the trends in radial velocity with y, which resemble the rotation curves of known spirals (e.g. Rubin et al. 1985).

For each galaxy, we measure the difference in maximum and minimum line λ across the spectrum, and in Table 8 give the corresponding radial velocity difference, Δv. This shows some correlation with luminosity (correlation coefficient 0.69), with a best-fit power law $\log \Delta v = -0.3429 M_B - 5.501$ (Figure 16). The power-law is steeper than for σ_i, but the two velocities are about equal for the more luminous galaxies ($M_B \simeq -22.5$). Much of the scatter
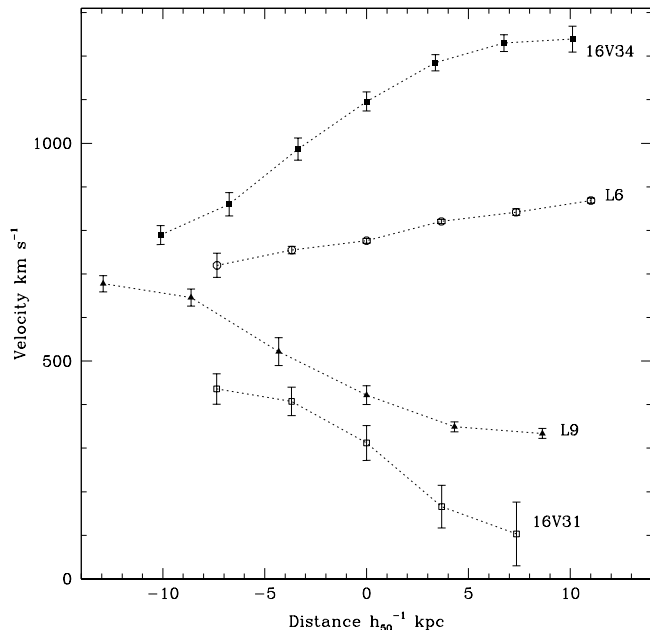
Figure 15. Rest-frame radial velocity (arbitrarily offset on the y axis) as measured from the centroid of the strongest emission line, as a function of distance across the galaxy (in h_{50}^{-1} kpc), for four rotating galaxies.

Figure 16. The radial velocity shift across each galaxy, Δv, plotted against blue absolute magnitude M_B. The dotted line is the best-fit power-law. The dashed lines show the mean relations of rotation velocity to M_B for Sa, Sb and Sc spirals, from Rubin et al. (1985)

$\sigma(\log \sigma_i) = 0.41$ is undoubtedly due to the random orientations – 16V34 and 16V31 appear almost optimally aligned while e.g. 16V15 and 16V25 are almost face-on, and in 16V36 the slit passes through only one of the two nuclei.

Again the v_{rot}–M_B relations of Rubin et al. (1985) are plotted. About 8 or 9 of the 14 galaxies are consistent with these, assuming $\Delta v \sim v_{rot}$. The steepness of our fitted correlation, compared to the ~ 0.1 slope of these single-type relations, is most likely due to the lower luminosity galaxies in our sample being later Hubble types and/or HII galaxies.

We conclude that 12/14 galaxies are consistent with spiral kinematics, while the low-luminosity 16V22 and L24 are low in both σ_i and Δv and appear more consistent with HII galaxies (Guzmán et al. 1997). None of these 14 show the kinematics of normal giant ellipticals, which have high velocity dispersions, $\sigma_i \simeq 250$ km s^{-1}, but much lower rotation velocities, $0 < v_{rot} < 0.4\sigma_i$. S4, although bulge-profile, gave a high Δv which might be evidence of an ongoing merger.

10 DISCUSSION – THE NATURE OF $\sim 10\mu$JY SOURCES

10.1 Comparison with Hammer et al. (1995)

Hammer et. al. (1995) investigated a sample of galaxies to slightly shallower but comparable limits of $F(5.0 \text{ GHz}) \simeq 16\mu$Jy and $I_{AB} = 22.5$. Firm spectroscopic IDs included one QSO, a possible radio galaxy, 5 ellipticals, 6 spirals and 5 emission-line galaxies. Their results agree with ours in that the most prominent type of galaxy were $L \geq L^*$ spirals, with moderate [OII] emission and often Balmer absorption lines.

Hammer et al. (1995) report a higher proportion of ellipticals than our 3/27, but 3 of their 5 spectroscopically confirmed ellipticals are at $z = 0.99$, suggesting the elliptical fraction is enhanced by a cluster. There is evidence that $z \geq 1$ ellipticals are even more clustered than the present-day E/S0 population (Daddi et al. 2000), so large field-to-field variations in their numbers would be expected. Furthermore, at the less deep radio flux limit of Hammer et al., radio-luminous ellipticals (AGN) are likely to be more numerous relative to star-forming galaxies.

Of the 5 galaxies described by Hammer et al. as 'emission-line', 4 are sub-L^* galaxies with line ratios more consistent with Seyferts or LINERs than pure starbursts. In contrast, we concluded that our two sub-L^* galaxies had line ratios within the range of HII galaxies. However, these variations are not surprising considering that line-ratio diagnostic plots show a great concentration of low-luminosity galaxies around the HII/Seyfert/LINER dividing node (Tresse et al. 1996). The fifth is a high redshift ($z = 1.16$) galaxy, with strong [OII] emission and no direct evidence for an AGN, and might be similar to our S10.

10.2 'Normal' Galaxies

Some ~ 20 per cent of our sample consists of apparently 'normal' galaxies at lower redshifts. The disk galaxies 16V28, 16V29, L13 and L15 and the elliptical S11, are optically bright ($R < 19$), low redshift ($z_{mean} = 0.15 \pm 0.05$), $L \sim L^*$ luminosity galaxies with relatively low radio/optical flux ratios, consistent with non-starburst spirals or normal E/S0s. None appear visibly disturbed or interacting.

10.3   QSOs

Some ~ 15 per cent of the sources are identified from their spectra as QSOs. These sources, 16V13, 16V17, L5 and L17, are all high redshift ($1.6 < z < 2.6$), optically very luminous ($M_B \sim -25.5$) objects with starburst-like $B - R$ colours. 16V17, L4 and L17 appear stellar and have relatively moderate radio/optical flux ratios, intermediate between the normal and starburst galaxies.

The QSO 16V13 differs from the others in that (i) its radio/K band luminosity ratio is a factor ~ 8 higher (Figure 10), (ii) optical and K' images show the compact bright source to be associated with a lower surface brightness 'tail' and three blue ($B - R \simeq 0.3$) companion galaxies; (iii) the spectrum shows a doublet of very strong (EW $\simeq 16$–19Å) narrow MgII absorption lines, and (iv) Windhorst et al. (1993) found the radio source to be extended – elongated by 12.6 ± 3.0 arcsec on a position angle $133° \pm 25$. It may therefore be a more complex object, e.g. a radio QSO with jet-triggered star-formation. If the radio emission is primarily from starbursting, the Dunne, Clements and Eales (2000) relation of $F(850\mu m)/F(/1.4$ GHz$)$ to z for star-forming galaxies predicts $F(850\mu m) \simeq 17$mJy, which would be easily detectable with SCUBA.

10.4   Obscured AGN (probable)

Two of the three ellipticals, S4 and S5, have a very high $L_{8.44}$, which if due to star-formation, would require SFR $\geq 1000 M_\odot yr^{-1}$. These galaxies appear to be regular giant ellipticals without visible point-sources or knots. It seems more likely that their radio emission is produced by obscured AGN. Radio bursts from AGN may be triggered by even minor interactions. S5 appears to be the central galaxy of a group or cluster (Weistrop et al. 1987), with a much smaller dwarf galaxy ~ 40 kpc from the nucleus. S4 is not visibly interacting on these images, but its spectrum showed a high velocity gradient, which may be evidence for an interaction.

It is also possible that 16V10* contains a radio AGN, as it has a similarly high $L_{8.44}$ and the radio source is reported to be elongated (Windhorst et al. 1993).

10.5   Starburst Galaxies

More than half of our sample consists of disk galaxies with high radio luminosities, suggesting powerful ($\sim 100 M_\odot yr^{-1}$) starbursts; 16V15*, 22, 25, 31, 34, 36, L3, L6, L18, L19, L21, L24, S10 and possibly 16V10*. The radio/K luminosity ratio – an approximate indicator of the ongoing/recent SFR relative to the total stellar mass – varies greatly (~ 2.5 dex) within the sample as a whole, is not obviously correlated with optical luminosity, and its distribution extends ~ 1.5 dex above a constant-SFR model (Figure 10). This appears to reflect the underlying distribution of starburst intensities, as the optically-based Guzmán et al. (1997) plot of SFR/mass against galaxy mass is very similar.

Interactions: Interaction-triggered starbursts appear to be the primary cause of enhanced radio emission from disk galaxies. We identify 11 of our redshift sample as being in close pairs, and several others appear disturbed. For one pair, 16V15*/16V15B, we have spectra for both components, confirming the redshifts are the same; another galaxy,

16V36, has prominent tidal tails and a double nucleus, leaving no doubt that it is a merger. S10, with the strongest emission lines, is very asymmetric – the nucleus is off-centre by $\sim 1/4$ of the semi-major axis – almost certainly from an interaction.

Serjeant et al. (2000) imaged four radio-selected starburst galaxies at $z \sim 0.2$ with WFPC2, and found all four to be interacting or disturbed, and two to be very asymmetric. On this basis it is likely that higher resolution imaging would reveal evidence of interaction in other galaxies in our sample.

The mean projected separation of the pairs is a relatively wide $36 \pm 5 h_{50}^{-1}$ kpc, which implies that, in many mergers, the SFR and radio emission peak well before nuclear coalescence (36 kpc is 117 Myr at 300 km s^{-1}). The wide range of separations is consistent with merger simulations where the maximum SFR may occur at nuclear coalescence or several $\times 10^8$ yr earlier, depending on the structure of the galaxies (Mihos and Hernquist 1996) and their relative orbital configurations (Bekki and Shioya 2000).

Excitation: We estimated the [OIII]5007 to Hβ flux ratio (excitation) for 9 of the galaxies, and found seven to have moderate excitations, averaging 0.51, implying the high ($Z \sim 1.1 Z_\odot$) metallicities of $L \geq L^*$ spirals. Two with lower optical luminosities ($M_B > -20$) have much higher excitations of ~ 2.8, consistent with low metallicity ($Z \sim 0.5 Z_\odot$) HII galaxies. This diversity of spectral types is similar to that in the Hammer et al. (1995) sample, although none of these 9 galaxies have the very high excitations (≥ 5) indicative of AGN. The metallicity – luminosity relation appears consistent with that of optically selected galaxies and hence with the radio sources being formed from 'normal' spirals and irregulars, e.g. through interactions.

Kinematics: Using the strongest emission lines in our spectra we estimated internal velocity dispersions and rotation velocities for 14 galaxies. Most of the sample were consistent with the kinematics ($v_{rot} \simeq 100$-400 km s^{-1}) of massive spirals. The lowest optical luminosity galaxies, 16V22 and L21 had much lower velocity dispersions and rotation velocities, < 60 km s^{-1}, consistent with low-mass HII starburst galaxies.

10.6   Radioluminous Starbursts: Dust and Age Effects

The SFRs estimated from radio luminosities are consistently about an order of magnitude higher than those indicated by the emission line (H_β and/or [OII]3727Å) luminosities. The most obvious explanation is dust extinction of the emission lines. The typical shortfall in H_β flux, interpreted in this way, implied $A(H\beta) = 1.9$–2.8 mag, with similar results for [OII]3727Å. This is a common finding in radio-luminous starbursts, e.g. Smith et al. (1996) found the ratio of Brγ ($2.166\mu m$) to thermal radio emission to be only 4–18 per cent of that exected without dust, in starburst galaxies (mostly interacting) of similar radio luminosity to our sample. Furthermore, in the 10 Wolf-Rayet galaxies of Beck, Turner and Kovo (2000), and the 4 starburst galaxies of Serjeant et al. (2000), the $H\alpha$ luminosities correspond to SFRs a factor ~ 10 lower than the radio luminosities.

Despite this, our radio IDs are not in general significantly redder than optically-selected galaxies (Figure 5),

and some have very blue, starburst colours. This discrepancy can be explained if the dust is inhomogeneously distributed and produces an 'age-dependent' extinction – several magnitudes for the most newly formed stars ($< 10^7$ yr), progressively decreasing for stellar populations of increasing age (e.g. Poggianti and Wu 2000; Poggianti et al. 2000; also the merger model of Bekki and Shioya 2001). $H\beta$ emission, tracing star-formation over the previous few Myr, would be greatly attenuated, whereas slightly older stars emerging from high-extinction regions can produce blue colours and, eventually, $H\delta$ absorption. Hence galaxies with ongoing, reddened starbursts could still appear very blue and may have e(a) spectra.

However, an estimate of dust extinction from $H_\beta/L_{8.44}$ would be strictly valid only if the SFR is relatively constant over $> 10^8$ yr, as a consequence of $L(H_\beta)$ and $L_{8.44}$ tracing star-formation over different timescales, < 7 Myr and ~ 70 Myr. Shorter starbursts would cause their ratio to fluctuate. Glazebrook et al. (1999) and Sullivan et al. (2000) find star-forming galaxies to show a very wide scatter in the ratio of H_α to UV continuum flux, and attribute this to most of the star-formation occurring in repeated ~ 50 Myr bursts. Thornley et al. (2001) report that variations in the mid-infra-red line ratios of starburst galaxies imply that the most massive stars are formed in even shorter (~ 10 Myr) bursts.

Sullivan et al. (2000) estimated SFRs from the UV continuum and $H\alpha$ luminosity of UV-selected galaxies. Even after taking into account a greater extinction for the star-forming nebulae (A_N) compared to the whole stellar population (A_s), assuming $A_s = 0.44 A_N$ (see Calzetti 1997), they consistently found the $H\alpha$-estimated SFRs to be lower than the UV estimates. In contrast, Glazebrook et al. (1999) had found the opposite result, higher $H\alpha$ SFRs, for optically-selected galaxies. The discrepancy was attributed to the wide intrinsic scatter in H_α/L_{UV} combined with selection effects. In the same way, a radio-selected sample may be biased towards a lower than 'normal' (i.e. steady-SFR) mean $H_\beta/L_{8.44}$, by the inclusion of many recent post-starbursts.

In our spectroscopic sample we identify 3 'e(a)' galaxies, L9, L18 and 16V31, out of 7 where the observed λ range would include $H\delta$ (Table 2). This fraction of e(a) galaxies is similar to that in the Hammer et al. (1995) survey, and also with the ~ 40 per cent estimated by Poggianti and Wu (2000) for optically selected merging/interacting galaxies (compared to 7–8 per cent in typical field galaxies). The low $H_\beta/L_{8.44}$ of the e(a) galaxies might be explained if they are recent post-starbursts with a small amount of ongoing star-formation. However, galaxies with active starbursts, indicated by $H\gamma$ emission and/or strong oxygen lines (16V22, L21, S10), have similarly low $H_\beta/L_{8.44}$ ratios, as do the starburst Wolf-Rayet galaxies of Beck et al. (2000). This implies that, while burst-age effects may be significant, dust extinction of star-forming regions remains the dominant effect in reducing the average $H_\beta/L_{8.44}$.

Mid infra-red spectroscopy could potentially separate these effects by providing a virtually dust-independent diagnostic of starburst ages (Thornley et al. 2001), while Chandra observations of faint radio sources could identify which have contributions from obscured AGN (which produce elevated X-ray to radio flux ratios).

APPENDIX 1: ESTIMATING LUMINOSITIES

Optical Luminosity

We use the set of optical SEDs, from the Roche et al. (2001a) evolving models for normal galaxies , to 'de-k-correct' the apparent magnitudes and thus estimate absolute magnitudes in the rest-frame B and K' bands. For each model, we calculate two observer-frame to restframe corrections, $B_{rest} - R_{obs}$ and $K'_{rest} - K'_{obs}$, as a function of redshift. For each galaxy the appropriate correction is derived from its observed colour, as follows. The $B - R$ colour of each galaxy can be expressed as a combination of the two adjacent (i.e. one redder and one bluer) models at the same redshift. If the observed colour is C_g and the nearest redder and bluer models are C_r and C_b, then in the observed R band the fraction of the bluer model is $f_b = \frac{10^{-0.4C_g} - 10^{-0.4C_r}}{10^{-0.4C_b} - 10^{-0.4C_r}}$.

L3, for example, is intermediate between the Im and Burst models with $f_b = 0.35$. The restframe correction of the galaxy D_g is then estimated by interpolating between the restframe corrections of the two models at the same redshift, D_b and D_r, as: $D_g = 2.5 \log [f_b * 10^{-0.4D_b} + (1 - f_b) * 10^{-0.4D_r}]$.

This $B_{rest} - R_{obs}$ correction is then added to the observed R magnitude, and the distance modulus (for $\Omega_m = 0.3$ $\Omega_\Lambda = 0.7$) is subtracted to give an AB-system absolute magnitude in the rest-frame blue-band, M_B ($+ 5 \log h_{50}$). The $R - K$ colour of each galaxy can similarly be expressed as a combination of two adjacent models, giving a ratio of the two models in the K'-band, which is used to interpolate, giving a correction $K'_{rest} - K'_{obs}$. This is added to K', and the distance modulus subtracted, to give M_K.

Radio Luminosity

The restframe 8.44 GHz luminosity (hereafter $L_{8.44}$), in the form νL_ν ergs s^{-1}, is estimated as
$\log L_{8.44} = 40.08 - 23.0 + \log (8.44 \times 10^9) + 0.4 \, d_{mod} + 0.4 \, k_{8.44} + \log F(8.44)$
where d_{mod} is the distance modulus in magnitudes, $F(8.44)$ the observed 8.44 GHz flux in μJy, and $k_{8.44}$ the 8.44 GHz k-correction derived from the Condon (1992) radio SED,
$k_{8.44} = -2.5 \log[(1 + z) F_\nu(8.44[1 + z] \text{ GHz}) / F_\nu(8.44 \text{ GHz})]$
magnitudes.

Acknowledgements

REFERENCES

Bertin E., Arnouts S., 1996, A&AS 117, 393.

Beck S.C, Turner, J., Kovo O., 2000, AJ, 120, 244.

Bekki K., Shioya Y., 2000, A&A, 362, 97.

Bekki K., Shioya Y., 2001, ApJS, 134, 241.

Calzetti D., Bohlin R., Kinney, A. L., Storchi-Bergmann T., Heckman T. M., 1995, ApJ, 443, 136.

Calzetti D., 1997, AJ, 113, 162.

Carilli C.L., 2000. 'Starburst Galaxies near and far', eds. D. Lutz, L. Tacconi, Springer. (astro-ph/0011199)

Clements D. L., Sutherland W. J., McMahon R. G., Saunders W., 1996, MNRAS, 279, 477.

Condon J.J., 1992, A&A Ann. Rev., 30, 575.

Daddi, E. Cimatti A., Pozzetti L., Hoekstra H.. Röttgering H. J. A., Renzini A., Zamorani, G., Mannucci F., 2000, A&A, 361, 535.

Delgado R.M., Leitherer C., Heckman T., 1999, ApJS, 125, 489.

Dunne L., Clements D.L., Eales S., 2000, MNRAS, in press.

Flores H., Hammer F., Desert F. X., Césarsky C., Thuan T., Crampton D., Eales S., Le Fèvre O., Omont A., Elbaz D., 1999a, A&A, 343, 389.

Flores H., Hammer F., Thuan T., Césarsky C., Desert F. X., Omont A., Lilly S. J., Eales S., Crampton D., Le Fèvre O., 1999b, ApJ, 517, 148.

Fioc M., Rocca-Volmerange B., 1997, A&A, 326, 950.

Fioc M., Rocca-Volmerange B., 1999, (astro-ph/9912179).

Franx M., Illingworth G., Heckmann, T., 1989, AJ, 98, 538.

Fukugita M., Shimasaku K., Ichikawa T., 1995, PASP, 107, 945.

Gallego J., Zamorano J., Rego M., Vitores A.G., 1997, 475, 502.

Glazebrook K., Blake C., Frossie E., Lilly S., Colless M., 1999, MNRAS, 306, 843.

Guzmán R., Gallego J., Koo D.C., Phillips A., Lowenthal J., Faber S., Illingworth G., Vogt N., 1997, ApJ, 489, 559.

Haarsma D.B., Partridge R.B., Windhorst R.A., Richards E.A., 2000, ApJ, 544, 641.

Hammer F., Crampton D., Lilly S. J., Le Fèvre O., Kenet T., 1995, MNRAS, 276, 1085.

Hammer F., Flores H., Lilly S. J., Crampton D., Le Fèvre O., Rola C., Mallen-Ornelas G., Schade D., Tresse L., 1997, ApJ, 481, 49.

Hanlan P., Bregman J., 2000, ApJ, 530, 213.

Holtzman J., Watson A., Baum W., Grillmair C., Groth E., Light R., Lynds R., O'Neil E., 1998, AJ, 115, 1946.

Kennicutt R.C., 1983, ApJ 272, 54.

Kennicutt R.C., 1992, ApJ, 388, 310.

Kobulnicky H.A., Koo D.C., 2000, ApJ, 545, 712.

Koo D.C., Guzmán, Faber S., Illingworth G.D., Bershady M.A., Kron R.G., Takamiya M., 1995, ApJ, 440, L49.

Le Fèvre, et al., 2000, MNRAS, 311, 565.

Lisenfeld U., Völk H., Xu C., 1996, A&A, 314, 745.

Mallen-Ornelás G., 2000, Ph.D. Thesis, University of Toronto.

McCall M.L., Rybski P.M., Shields G.A., 1985, ApJS, 57, 1.

Matthews K., Soifer B.T., 1994, ExA, 3,77.

Melnick J., Terlevich R., Moles M., 1988, MNRAS, 235, 297.

Mihos J.C., Hernquist L., 1996, ApJ, 464, 641.

Mobasher B., Cram L., Georgakakis A., Hopkins A., 1999, MNRAS, 308, 45.

Munn J.A., Koo D.C., Kron R., Majewski S., Bershady M., Smetanka J., 1997, ApJS 109,45.

Niklas S., Klein U., Wielebinski R., 1997, A&A, 322, 19.

Oke J.B., et al., 1995, PASP, 107, 37.

Pastoriza M.G., Donzelli C.J., 2000, AJ, 129, 189.

Poggianti B., Bressan A., Franceschini A., 2001, ApJ, 550, 195.

Poggianti B., Wu H., 2000, ApJ, 529, 157.

Richards E. A., Kelloman K., Fomalont R., Windhorst R., Partridge R., 1998, AJ, 116, 1039.

Rix H.-W., Guhathakurta P., Colless M., Ing K., 1997, MNRAS, 285, 779.

Roche N., Eales S., 2000b MNRAS, 317, 120.

Roche N., Eales S., Matthews J., Maugham B., 2001a, MNRAS, submitted.

Rubin V.C., Burstein D., Ford W.K., Thonnard N., 1985, ApJ, 289, 81.

Rudnick G., Rix H.-W., Kennicutt R.C., 2000, ApJ, in press.

Rush B., Malkan M. A., Spinoglio L., 1993, ApJS, 89, 1.

Schmitt H. R., Kinney A. L., Calzetti D., Storchi-Bergmann T., 1997, AJ, 114, 592.

Serjeant S., Mobasher B., Carlotta G., Oliver S., 2000, MNRAS, 317, L29.

Smith D., Herter T., Haynes M., Beichman, C., Gautier T., 1996, ApJS, 104, 217.

Smith D., Herter T., Haynes M., 1998, ApJ, 494, 150.

Sodré L., Stasinska G., 1999, A&A, 345, 391.

Sullivan M., Treyer M. A., Ellis R.S., Bridges T.J., Milliard B., Donar I., 2000, MNRAS, 312, 442.

Telles E., Terlevich R., 1993, Ap$SS, 205, 59.

Thornley, M., Schreiber, N.M.F., Lutz, D., Genzel R., Spoon, H.W.W., Kunze, D., Sternberg, A., 2000, ApJ 439, 641.

Tresse L., Rola C., Hammer F., Stasinska G. Le Fevre O., Lilly S.J., Crampton D., 1996, MNRAS, 281, 847.

Vogt N.P., Forbes D., Phillips A., Gronwall C., Faber S., Illingworth G., Koo D.C., 1996, ApJ, 465, L15.

Weistrop D., Wall J., Fomalont E.B., Kellermann K., 1987, AJ, 93, 805.

Windhorst R.A., Fomalont E.B., Kellermann K.I., Partridge R.B., Richards E., Franklin B.E., Pascarelle S.M., Griffiths R.E., 1995, Nature, 375, 471.

Windhorst R.A., Fomalont E.B., Partridge R.B., Lowenthal J.D., 1993, ApJ, 405, 498.